Cell Reports
Physical Science

CellPress
OPEN ACCESS

Article

Accelerated impedance-based aging modeling for NCA/Gr-SiOx batteries and the impact of reduced test duration

Ahmed Chahbaz,[1,3,4,6,*] Markus Schreiber,[2] Jonas Rinner,[1,3,4] Joaquín Mascareñas Hinojosa,[1,3,4] Gereon Stahl,[1,3,4] Markus Lienkamp,[2] and Dirk Uwe Sauer[1,3,4,5]

[1]Chair for Electrochemical Energy Conversion and Storage Systems, Institute for Power Electronics and Electrical Drives (ISEA), RWTH Aachen University, Campus-Boulevard 89, 52074 Aachen, Germany

[2]Technical University of Munich (TUM), School of Engineering & Design, Department of Mobility Systems Engineering, Institute of Automotive Technology, Munich, Germany

[3]Jülich Aachen Research Alliance, JARA-Energy, Templergraben 55, 52056 Aachen, Germany

[4]Center for Aging, Reliability and Lifetime Prediction of Electrochemical and Power Electronic Systems, RWTH Aachen University, Campus-Boulevard 89, 52074 Aachen, Germany

[5]Helmholtz Institute Münster (HI MS), IEK 12, Forschungszentrum Jülich, 52425 Jülich, Germany

[6]Lead contact

*Correspondence: ahmed.chahbaz@isea.rwth-aachen.de

https://doi.org/10.1016/j.xcrp.2025.102654

SUMMARY

Aging models are essential for evaluating the aging behavior of lithium-ion batteries (LIBs) and guiding industry decisions on warranty commitments. This study presents an open-source impedance-based aging model for a nickel cobalt aluminum/silicon oxide-graphite LIB. The model accurately predicts capacity loss across various stress factors, achieving less than 1% deviation from validation measurements in real-world driving scenarios. Traditional modeling approaches require extensive testing and parameterization, making the assessment of new cell designs time consuming and costly. To address this issue, optimized testing strategies are developed through sensitivity analysis, revealing significant potential to reduce testing efforts by focusing on key stress factors such as temperature for calendar aging and depth of discharge for cyclic aging. Additionally, using fractional portions of available aging data suggests that test durations of 90 days may be sufficient to achieve reliable results.

INTRODUCTION

Emission-reducing innovations, especially in the field of battery-powered mobility, have been subject to many applications and studies in recent years.[1,2] High energy and power density, high charge and discharge efficiency, low self-discharge rate, and low maintenance costs have made the lithium-ion battery (LIB) technology predominant in the field of large-scale applications such as electric vehicles (EVs) and stationary storage systems (ESSs).[3,4]

Electrochemical systems, such as LIBs, are inherently subject to degradation. This degradation is reflected in a capacity loss and an increase in internal resistance, resulting in decreased energy and power capabilities.[5] A comprehensive understanding of the performance of LIBs is essential for their widespread application. However, testing every possible degradation path requires considerable time and testing resources. Consequently, battery models capable of predicting and optimizing battery performance under diverse operating conditions are crucial for the development of efficient, safe, and reliable battery systems, ultimately reducing development costs. Among data-driven and electrochemical models,[6–8] impedance-based aging models are widely known to strike an optimal balance between model accuracy and complexity in terms of parameterization and computation effort.[9] While electrochemical models provide more detailed insights into the individual cell reactions that govern battery aging, impedance-based models offer practical advantages in terms of simplicity, efficiency, and system-level analysis. State-of-the-art impedance-based aging models serve as a widely utilized diagnostic tool in various applications to assess the state of charge (SOC) and state of health (SOH) of LIBs within their respective operational contexts.[10,11] This is achieved through electrical circuit models (ECM), which offer the capability to replicate the non-linear voltage response of LIBs. Their parameterization relies on dedicated measurements such as electrochemical impedance spectroscopy (EIS) or pulse measurements, which are effective non-invasive methods for characterizing the polarization behavior of LIBs across a wide frequency range and time domain, under the influence of various parameters such as temperature and SOC.[12,13] Besides diagnostics, impedance-based aging models can be utilized to optimize operating conditions for different application scenarios through aging prediction, which can enhance the overall profitability of a battery system. Rather than focusing on microscopic

aging mechanisms, e.g., lithium plating,[14] solid electrolyte interface (SEI) growth,[15] or particle cracking,[16] impedance-based aging models focus on macroscopic stress factors, e.g., depth of discharge (DOD), SOC, current rate (C-rate), temperature, or pressure[17–22] and differentiate their respective contributions into two separate components, calendar and cyclic aging.[23,24] Extensive literature exists on the development and parameterization of ECMs for different application scenarios.[25–31] Nevertheless, only a few studies couple these ECMs with aging models.[32–34]

Based on the available literature, two key points can be deduced. First, it is evident that current modeling approaches predominantly focus on LIBs with purely graphite (Gr)-based anodes. However, as future developments increasingly incorporate silicon fractions in anodes, new challenges emerge during modeling.[35] The literature on developing impedance-based aging models for these newer cell chemistries is limited, primarily due to challenges arising from the significant hysteresis behavior of silicon that can lead to accelerated aging when cycling is performed within specific SOC regions where the silicon particles experience a notable volume expansion.[36–39]

Second, due to the extensive testing capacities and time commitments required, the literature on sophisticated aging models that consider multiple stress factors and validation measurements conducted under real-world operating conditions remains limited. To reduce testing efforts and accelerate the model-acquisition process, various approaches have been proposed. It is well established that although incorporating a greater number of stress factors into an aging model enhances the accuracy of estimated results, it concurrently increases the necessary testing capacities and time commitments involved.[40] Therefore, testing efforts can be minimized by focusing on aging components that predominantly influence overall aging within the specific operational scenarios being investigated. Several studies advocate for solely examining calendar aging while overlooking cycle aging.[41–43] Although it may be suitable to only consider calendar aging for certain applications with specific requirements, such as for deep space missions[44,45] or military operations,[46] the impact of fast charging[47] and deep cycling[48] must be considered to cover alternative extreme operational scenarios that can significantly impact overall aging. Particularly for LIBs with advanced cell chemistries containing fractions of silicon in the anode, cyclic aging impacts overall lifetime even more profoundly within specific cycle regions.[49,50] Another strategy to accelerate the model-acquisition process involves conducting accelerated tests under pronounced stress conditions, such as elevated ambient temperatures or increased C-rates. The models presented by Schmalstieg et al.[32] and Sarasketa-Zabala et al.[33] demonstrated robust predictive capabilities for capacity loss that align closely with validation measurements, despite being parameterized using datasets obtained under conditions designed to accelerate aging. In this context, we investigate how the test duration in accelerated calendar and cyclic aging tests fundamentally affects model accuracy. This approach can ultimately lower costs associated with evaluating new cell designs, thereby enabling faster decision-making in the production process of LIBs.

This paper presents the development, parameterization, and validation of an impedance-based semi-empirical aging model for a commercially available LIB featuring a silicon oxide (SiOx)-Gr blend anode using open-source-available tools. The final model along with all utilized tools are publicly accessible for use by industry and research institutions. The development of the ECM for the studied cell is illustrated through the use of EIS and pulse measurements, with distribution of relaxation times (DRT) serving as an analytical tool to derive significant insights into the complexity of the chosen ECM. Additionally, a hysteresis model is presented and integrated to account for the pronounced hysteresis effects of silicon, particularly in low-SOC regions. Consequently, our paper serves as a blueprint for researchers aiming to replicate our methodology for their own cell designs. Following the validation of the electrical model, a semi-empirical aging model based on aging measurements conducted on more than 50 cells is presented and validated across various real-world operating scenarios. To investigate strategies to reduce testing time, a sensitivity analysis is performed to identify critical stress factors. Following this analysis, the aging model is refitted using fractional portions of the total available calendar and cyclic aging data, with the aim of identifying the shortest test duration necessary to achieve acceptable model estimations.

RESULTS AND DISCUSSION

Analysis of impedance characteristics

The EIS measurements obtained at temperatures of 5°C and 45°C are illustrated in Figures 1A and 1B. The EIS measurements corresponding to the other investigated temperatures at 15°C, 25°C, and 35°C can be found in Figure S1. The results are presented in the form of Nyquist plots for each measured temperature with a SOC value ranging from SOC = 0% to SOC = 100% with $\Delta SOC = 10\%$. Figures 1C and 1D provide a direct comparison of the measured impedance spectra at different temperatures with fixed SOC levels of 0% and 100%, highlighting the temperature dependency at a specific SOC level. The inspection of the measured impedance reveals three distinct frequency regions, as labeled in Figure 1A.

(1) High frequency (HF): In the HF region (6–1 kHz), the presence of inductive influences ($\mathrm{Im}(Z) > 0$) in the impedance primarily stems from the wounded cell geometry and its wiring.[51,52] Additionally, the impedance value in the frequency range where $\mathrm{Im}(Z) = 0$ is associated with the ohmic resistance contributions from the electrolyte, separator, and contact resistance between either the electrode/current collector or particle/particle interface.[29,31,52]
(2) Intermediate frequency (IF): The compressed semi-arc observed at intermediate frequencies (1 kHz to 0.1 Hz) reflects the impeded interfacial charge-transfer processes between the electrolyte/electrode interface and/or surface film impedances such as SEI or cathode electrolyte interface (CEI).[29,31,53]
(3) Low frequency (LF): The branch, observed at low frequencies (0.1–0.01 Hz), is ascribed to the solid-phase diffusion process.[54,55]

Based on the qualitative inspection of the presented EIS measurements in Figures 1A–1D, the impedance characteristic at

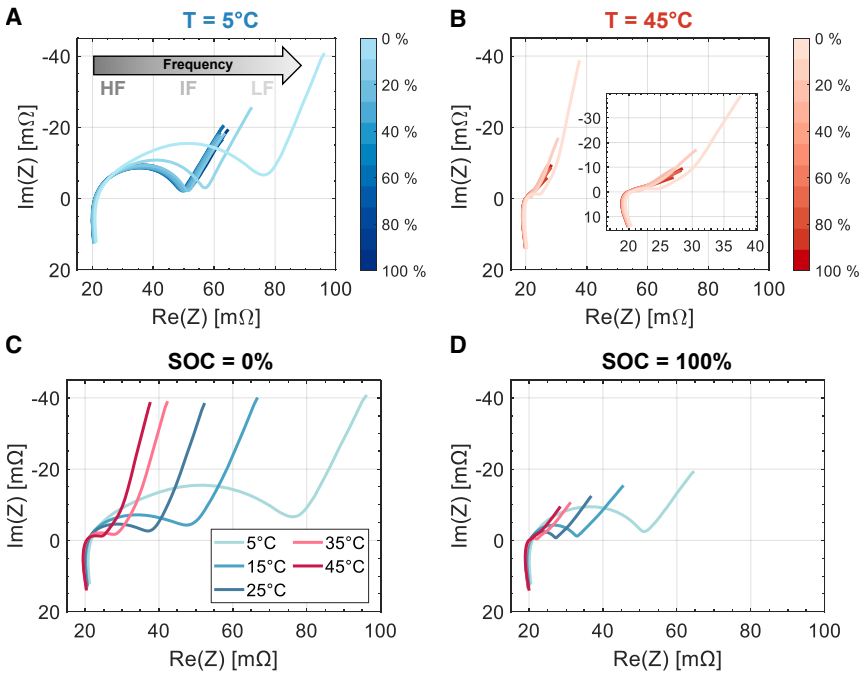

Figure 1. Analysis of the impedance characteristics under different temperatures and SOCs

(A and B) Nyquist plots of the obtained EIS measurements for SOCs ranging from 0% to 100% with 10% increments for (A) T = 5°C and (B) T = 45°C.

(C and D) Nyquist plots at fixed SOC levels for varying temperatures ranging from 5°C to 45°C for (C) SOC = 0% and (D) SOC = 100%.

different SOCs and temperatures can be directly assessed. The intersection between the x axis and the impedance spectra at HFs slightly shifts toward higher values with decreasing SOC, indicating an increase in ohmic resistance with decreasing SOC. Similarly, the width of the semi-arc observed at IFs increases significantly at lower SOC levels, while it only presents a slight decrease for SOCs above 10%. The temperature dependency can be assessed from Figure 1C. It is observed that the semi-arc at IFs increases significantly with decreasing temperatures, indicating impeded charge transfer at low temperatures.

Identification of main impedance contributions

It becomes evident that a separate quantitative analysis of the physical polarization contributions in the Nyquist plots is difficult, due to overlapping processes at different frequencies. Especially the physical processes contributing at IFs are not distinguishable and perceived as a single compressed semi-arc. Hence, an alternative analysis approach with increased resolution becomes necessary to interpret the measured EIS data and to separate the processes overlapping in the impedance spectra. Consequently, the DRT of the measured impedance spectra is examined.

The calculated DRTs for the corresponding previously presented EIS measurements in Figure 1 are depicted in Figures 2A–2D. The calculated DRT corresponding to the other investigated temperatures at 15°C, 25°C, and 35°C can be found in Figure S2. The DRT indicates five clearly distinguishable peaks labeled P1–P5 in Figure 2A. As mentioned in the methods section, the inductive behavior at HFs is accounted for by fitting an additional inductance, while the capacitive blocking electrode behavior at LFs is not quantitatively evaluated. Hence, this part is shaded gray in all DRT plots.

Each peak in the DRT corresponds to a physical process contributing to the overall cell polarization. The individual peaks can be assigned to corresponding physical processes based on the frequency range of their occurrence and their temperature/SOC dependency.[52,53] However, the statements made should be generally taken with caution, as not all specific internal cell processes can be mapped with certainty using only non-invasive techniques, due to the large number of electrochemical processes occurring within complex systems. Nevertheless, DRT serves as a valuable tool for determining the occurrence and amount of processes, their contribution to the overall impedance, and their temperature and SOC dependency.

The peak P_1 observed at HFs between 10^4 and 10^3 Hz is independent of SOC, as indicated by the absence of a change in the characteristic center frequency or a change in intensity over the entire SOC range in either of Figures 2A and 2B. However, a slight temperature dependency is observed, as shown in Figures 2C and 2D. Especially at higher temperatures above 35°C, a decrease in the intensity of peak P_1 is observed, while almost no change in intensity can be seen for temperatures below 25°C. Given that electrochemical processes typically do not take place at these elevated frequencies, P_1 is attributed to contact resistances at the particle/particle interfaces or the electrode/current collector interface, which is virtually unaffected by SOC and temperature variations according to several studies.[30,53,55]

It is evident that the processes occurring in the IF ranges exhibit a clear separation, perceived in the Nyquist plot only as a single semi-arc. Peak P_2 observed at IFs between 10^3 and 10^2 Hz demonstrates a distinct behavior. At lower SOCs, especially at SOC = 0%, P_2 shifts toward lower frequencies and the intensity increases significantly, as can be clearly seen in Figure 2A. Furthermore, a clear temperature dependency is observed, with P_2 disappearing almost completely at high temperatures above 35°C, while at lower temperatures P_2 constitutes a dominant portion of the overall cell impedance, as depicted in Figures 2C and 2D. Figure 2D reveals that for SOC = 100% above 25°C, P_2 partly overlaps with P_1, while at 15°C P_2 starts to become clearly distinguishable and shifts toward lower frequencies. The

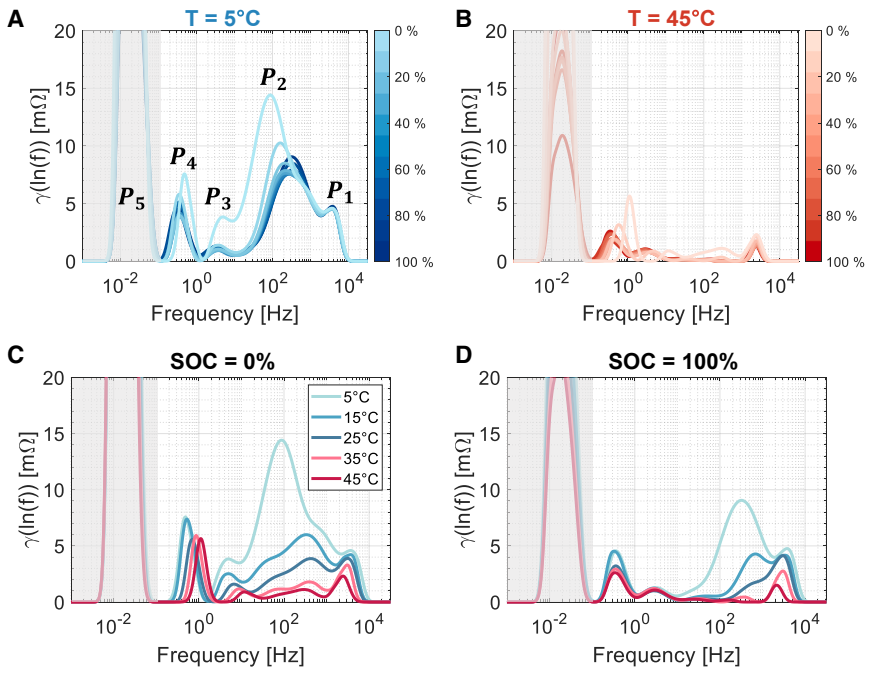

Figure 2. Analysis of the DRT characteristics at varying temperatures and SOCs

(A and B) Calculated DRT plots for SOCs ranging from 0% to 100% in 10% increments at fixed temperatures of (A) T = 5°C and (B) T = 45°C.

(C and D) DRT plots illustrating temperature variations from 5°C to 45°C at fixed SOC levels for (C) SOC = 0% and (D) SOC = 100%.

observed behavior within this frequency range indicates potential influences from the impedances associated with passivation films, which could originate from either the anode, such as the SEI, or the cathode, such as the CEI. In general, the thickness of the CEI is less than that of the SEI, especially for a pristine cell.[13,56] Hence, P_2 is attributed to the impeded process of lithium transport through the SEI layer. The exhibited SOC and temperature dependency of P_2 demonstrates behavior similar to that in previous investigations on both Gr and SiOx anodes.[30,57,58]

Peak P_3 observed at IFs between 10 and 1 Hz does not contribute significantly to the overall polarization of the battery. Additionally, no significant change in either the center frequency or the intensity becomes visible at different SOCs or temperatures, apart from one exception. At SOC = 0%, the characteristic frequency of P_3 shifts toward higher frequencies and starts to partly overlap with P_2. This shift is also observed at increased temperatures, where the center frequency of P_3 shifts toward higher frequencies, as becomes visible in Figure 2C. Furthermore, the intensity increases significantly at low temperatures below 15°C, while no significant intensity changes become visible for temperatures above 25°C. Zhu et al.[59] investigated the processes that occur at low temperatures within LIBs using DRT. Their findings reveal that as the temperature decreases, the charge-transfer impedance at the anode experiences a notable increase, whereas at elevated temperatures its impact on the overall cell impedance diminishes considerably. Moreover, the frequency range observed for the anode charge-transfer resistance aligns with the frequency range observed in our study and various other investigations.[57,60,61] Therefore, it is assumed that P_3 reflects the charge-transfer process of the anode.

Similarly, the peak P_4, observed at IFs between 1 and 0.1 Hz shifts toward higher center frequencies, and the intensity increases with decreasing SOC. P_4 shows the largest contribution to the overall impedance at temperatures above 15°C. It is widely acknowledged that the charge-transfer process of the cathode is the most sluggish process in the IF range and therefore shows the lowest center frequency.[62] Previous studies[13,53] have indicated that for nickel cobalt aluminum (NCA), the charge-transfer process occurs between 0.4 and 3 Hz, which aligns with the process observed in our study. Hence, P_4 is attributed to the charge-transfer process of the cathode.

Additionally, a process at LFs below 0.1 Hz is identified and mainly attributed to the solid-phase diffusion process.[52] However, as mentioned previously, due to the limited reliability of DRT at LFs, no quantitative analysis is performed. Nevertheless, the awareness of another process occurring at LFs is integrated into the model.

The information obtained from the DRT evaluation serves as the basis for establishing reasonable modeling assumptions, which will be evaluated in the following section.

Advanced electrical circuit model development

Based on the previous evaluation of the DRT, a corresponding ECM is proposed. The model parameters for different frequency ranges are extracted from different types of measurements. Given the better separation of fast processes in the HF and IF ranges, EIS measurements are used to derive these parameters. However, due to the limited measurement time of the EIS spectra, time-domain measurements are used to parameterize the model parameters in the LF range. The software used to obtain the model parameters from EIS and time-domain measurements is developed at our institute (ISEA, RWTH Aachen University) and made publicly available.[63,64]

Modeling fast battery dynamics through EIS

The selected model for the cell under investigation, based on the prior evaluation of the DRT, is shown in Figure 3A. The ECM consists of an inductance that is intended to account for the HF behavior of the cell. The ohmic resistance is modeled using a serial resistance R_0. Each identified process in the DRT is mapped by means of a ZARC element, often referred to as an RQ

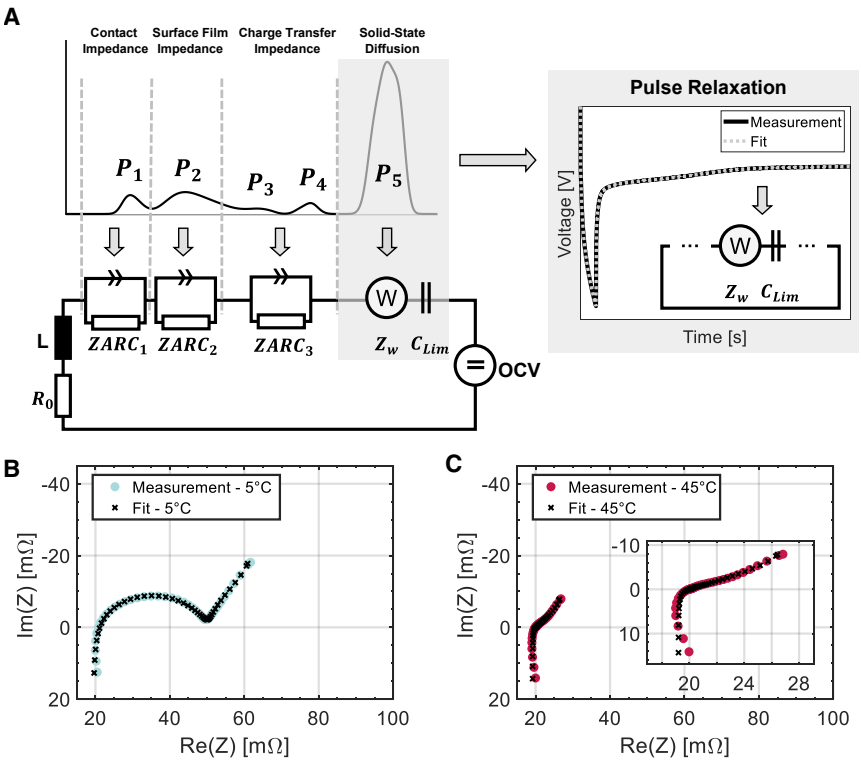

Figure 3. ECM development based on the DRT evaluation

(A) Assignment of different DRT processes to ECM parameters. The LF parts of the ECM are refitted using time-domain measurements.

(B and C) Comparison between measured impedance spectra and fitted ECM for (B) 5°C and (C) 45°C, both at fixed SOC = 50%.

element.[28,30] It is composed of a parallel connection of a constant phase element (CPE) and a resistance, defined as[65]

$$Z(j\omega) = \frac{R}{1+(j\omega\tau)^{\Phi}}. \quad \text{(Equation 1)}$$

In our model, only the polarization of the cathode charge transfer is considered using a ZARC element, as the anode charge-transfer resistance has an almost insignificant influence within the investigated temperature range to reduce model complexity. Accordingly, three ZARC elements $ZARC_1$–$ZARC_3$ are integrated into the used ECM to account for the contact, surface film, and charge-transfer impedance. The solid-state diffusion contributions occurring at LFs are modeled using a finite-length Warburg (FLW) element Z_W, similar to Gantenbein et al.[27] and Illig et al.[30] The used FLW is implemented as presented by Cruz-Manzo and Greenwood[66]:

$$Z(j\omega) = R_W \cdot \frac{\tanh\left(\sqrt{j\omega\tau_w}\right)}{\sqrt{j\omega\tau_w}}. \quad \text{(Equation 2)}$$

An additional capacity, C_{Lim}, is added in series to the FLW element to reflect the intercalation capacity, similar to the proposed approach by Levi and Aurbach.[67] The grayed-out elements in Figure 3A indicate the parameters that are later replaced by those parameters obtained from time-domain measurements. Finally, a voltage source is added to represent the open-circuit voltage (OCV) of the cell. The used ECM shows excellent agreement with the experimental data from the EIS measurements, as demonstrated in Figures 3B and 3C. The comparison between measured impedance spectra and fitted ECM for 15°C, 25°C, and 35°C can be found in Figure S3.

The obtained parameters for different temperatures and SOCs are displayed in Figure 4. The course of the ohmic resistance (R_0), the contact impedance (R_1), the film impedance (R_2), and the charge-transfer impedance (R_3) are displayed in Figures 4A–4D.

The ohmic resistance R_0, as depicted in Figure 4A, remains almost unchanged over the entire SOC range and only shows a small variation of approximately 1 mΩ within the SOC range of 0%–20% for all temperatures. In addition, R_0 has the lowest temperature sensitivity of all parameters with a parameter variation of less than 2 mΩ over a temperature change of 40 K. This indicates that the contribution of R_0 is decoupled of cell-internal occurring electrochemical reaction processes, as this would necessitate a much stronger SOC or temperature dependency.

The contact resistance R_1 does not show a significant deviation in magnitude across the SOC range between 20% and 80%, similar to R_0, as shown in Figure 4B. However, for SOCs below 20% a decrease in polarization becomes visible, which can be clarified by examining the processes that take place on a particle level. On the cathode, virtually no volume change is expected, while on the anode, the particle volume should be smallest in the fully delithiated state. As a result, the pore volume becomes largest at low SOCs, which consequently results in reduced contact resistance.

The surface film resistance R_2 in Figure 4C shows an exponentially decreasing trend with increasing SOC. Especially for SOCs below 20%, a significant increase of the surface film resistance becomes evident. It becomes visible that the surface film impedance is the dominant polarization contribution for temperatures below 25°C, which is in accordance with the results of Steinhauer et al.[57] This is also in accordance with the investigated DRT where, especially for low temperatures, a dominant polarization contribution of the surface film impedance became visible.

The charge-transfer resistance R_3, as illustrated in Figure 4D, exhibits an increase at high SOC levels above 80% across all temperatures. Typically, a U-shaped pattern is expected for the charge-transfer resistance, characterized by

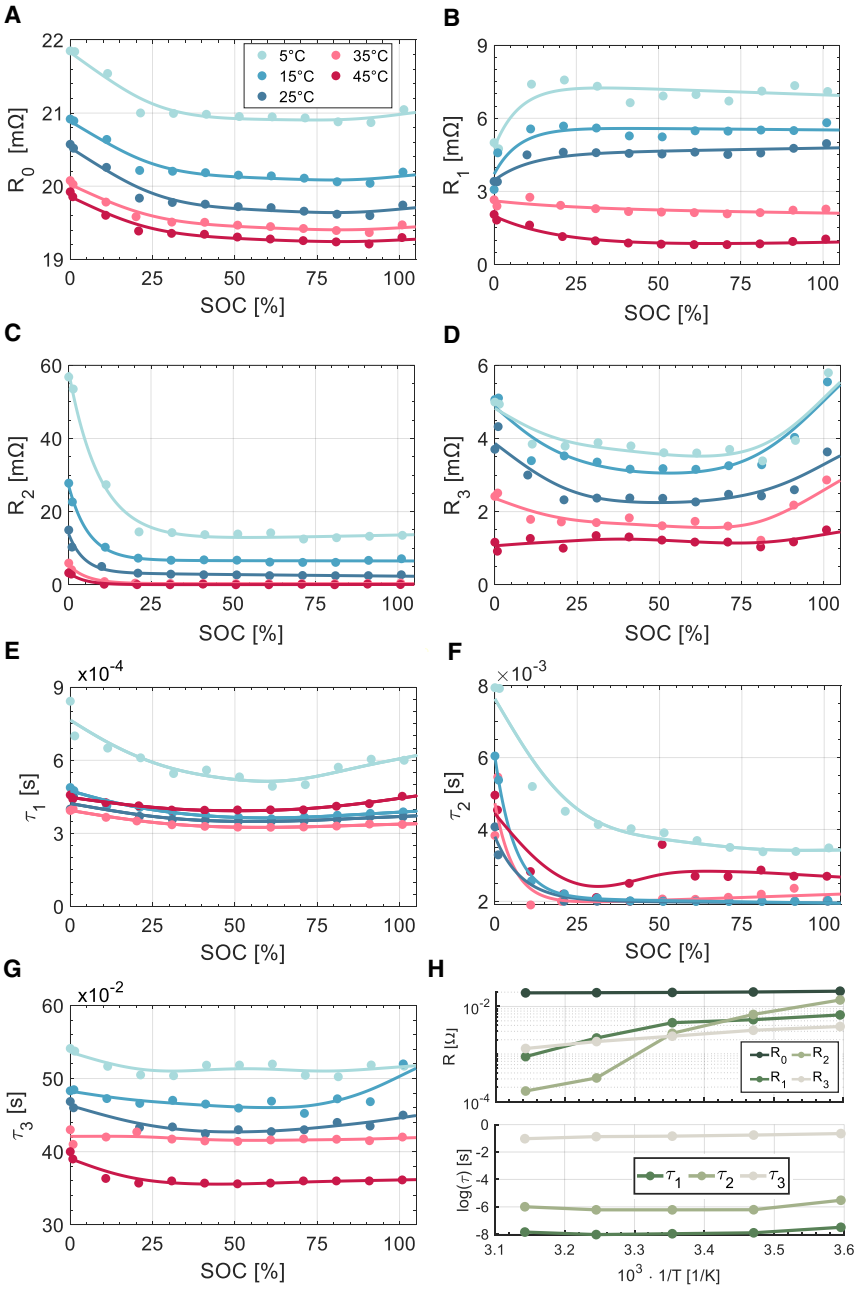

Figure 4. Fitted ECM parameters extracted from EIS measurements at varying temperatures and SOCs

(A) Ohmic resistance (R_0), (B) contact resistance (R_1), (C) surface film resistance (R_2), and (D) charge-transfer resistance (R_3). Corresponding relaxation times (E) τ_1, (F) τ_2, and (G) τ_3.

(H) Different impedance contributions and corresponding relaxation times at fixed SOC = 50% on a logarithmic scale over the inverse temperature.

high impedance values at both low and high SOCs, which aligns with findings from other studies.[53,68] However, in this case, lower impedance values are observed at low SOC levels, particularly at elevated temperatures. This behavior in NCA/Gr-SiOx batteries can be attributed to the silicon content in the anode, which inhibits the cathode from achieving high lithiation states that are usually associated with increased impedance values corresponding to low full-cell SOCs.[68] The hysteresis behavior primarily arising from the silicon content within the anode may lead to earlier reaching of the lower cutoff voltage, resulting in reduced lithiation of the cathode. To validate this hypothesis, more advanced *in situ* measurements at various SOCs, such as inductively coupled plasma or energy-dispersive X-ray spectroscopy analysis, are necessary. These investigations fall outside the scope of this paper but should be further explored in future studies.

The progression of the corresponding relaxation times τ_1–τ_3 are depicted in Figures 4E–4G. The relaxation times for the respective processes show a clear separation considering their magnitude but a corresponding proximity to each other when varying the SOC and temperature, indicating that, indeed, different processes have been fitted and, hence, with a physically plausible fit.

Figure 4H depicts the different impedance contributions and relaxation times for varying temperatures at a fixed SOC = 50% on a logarithmic scale over the inverse temperature. This is done to separately investigate the temperature dependency of the corresponding parameters. It becomes visible that all fitted impedance parameters show a clear temperature dependency, where decreased temperatures result in an increase of the respective polarization contribution, indicating again the physical plausibility of the fit.[30] R_2 exhibits the strongest temperature dependency, showing a variation of more than two decades over a temperature range of 40 K, while R_0 demonstrates the lowest temperature dependency due to its independence from electrochemical reactions, as previously described. Both R_1 and R_3 exhibit smaller temperature dependencies compared to R_2. This observation aligns with previous findings, where the contact and charge-transfer resistance displayed comparatively smaller temperature dependencies than the surface film resistance R_2.[30]

Modeling slow battery dynamics through time-domain measurements

The diffusion behavior of the battery was incorporated into the previously described model using an FLW. However, due to

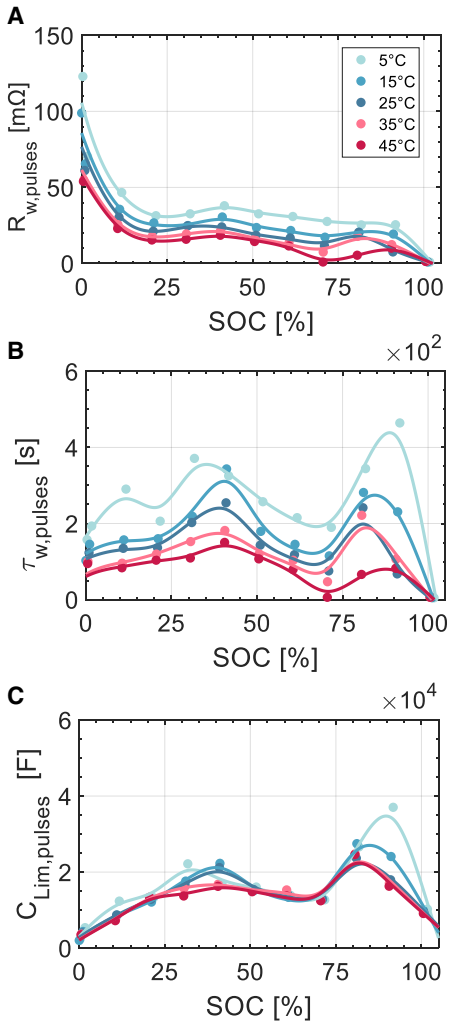

Figure 5. Fitted ECM parameters extracted from time-domain measurements at varying temperatures and SOCs

(A) Diffusion impedance ($R_{w,pulses}$).

(B) Corresponding diffusion relaxation time ($\tau_{w,pulses}$).

(C) Intercalation capacity ($C_{Lim,pulses}$).

the limited duration of the EIS measurements, the LF behavior cannot be fully mapped. Hence, slowly occurring processes with high relaxation times can be better analyzed using data obtained in the time domain. Therefore, based on the previously parameterized model for the HF and IF ranges derived from EIS measurements, the LF behavior of the battery is approximated using pulse-relaxation measurements.

A suitable measurement for parameter extraction is the voltage relaxation performed before each EIS measurement step when setting the SOC. The duration of the relaxation after discharge is designed to ensure that there is no significant voltage change at the end of the measurement, thereby covering all relevant LF model components. This approach is particularly efficient, since no additional measurement effort is required, due to the necessity of a relaxation period before performing an EIS measurement anyway.

The corresponding parameters are estimated for different SOCs and temperatures through an iterative fitting process, analogous to the parameter calculation from EIS measurements. It is important to note that only processes in the LF range are of interest during this step and are refitted using time-domain data. Differentiation between these parameters and those in the HF and IF ranges is achieved by considering the varying magnitudes of the obtained relaxation times, as indicated by the previously presented DRT analysis. Consequently, parameter values for all processes in the ECM with relaxation times $\tau < 1$ s are retained from the EIS fitting, while only the FLW and intercalation capacity are optimized using the time-domain fit.

The obtained model parameters for the LF region, namely $R_{w,pulses}$, $\tau_{w,pulses}$, and $C_{Lim,pulses}$, are shown in Figures 5A–5C. It becomes visible that the diffusion resistance shows a sharp increase at low SOCs. The trend of the respective model parameters are consistent for both parameterization methods, either through EIS or time-domain measurements. However, the magnitude of the relaxation time τ_w increases significantly, indicating that the fit using EIS measurements underestimates τ_w due to the limited duration of the measurement.

Advancing model precision for Gr-SiOx blend anodes via hysteresis modeling

In theory, the hysteresis of a LIB should be independent of any polarization effects and driven purely thermodynamically. However, in real operation, it is very difficult to achieve this thermodynamic equilibrium state, and hence a low-current measurement at C/50 is performed to achieve a quasi-equilibrium state.

Figure 6A depicts the charge (U_{CH}) and discharge (U_{DCH}) voltage of the investigated cell measured at 25°C in a quasi-equilibrium state with a low current of C/50. The average voltage (U_{AVG}) is also depicted and calculated as

$$U_{AVG} = \frac{U_{CH}+U_{DCH}}{2}. \quad \text{(Equation 3)}$$

It becomes evident that the cell exhibits different voltage characteristics, with U_{CH} being higher than U_{DCH}. The observed hysteresis characteristic is attributed to the SiOx content in the blend anode of the cell. Adding SiOx to the anode enhances the energy density, while intrinsic drawbacks come into play, including significant volume expansion of SiOx particles and substantial voltage hysteresis during the lithiation and delithiation process.[35,49,50]

Figure 6B depicts the hysteresis voltage between U_{CH} and U_{DCH}, according to

$$U_{\Delta} = U_{CH} - U_{DCH}. \quad \text{(Equation 4)}$$

The average hysteresis observed across SOC = 0%–100% amounts to 63.4 mV, with a maximum hysteresis voltage reaching 273.2 mV. This indicates that the hysteresis voltage associated with the blended anode is significantly higher than the reported average of pure Gr (~17 mV) but notably lower than that of pure SiOx (~266 mV).[69] Due to the

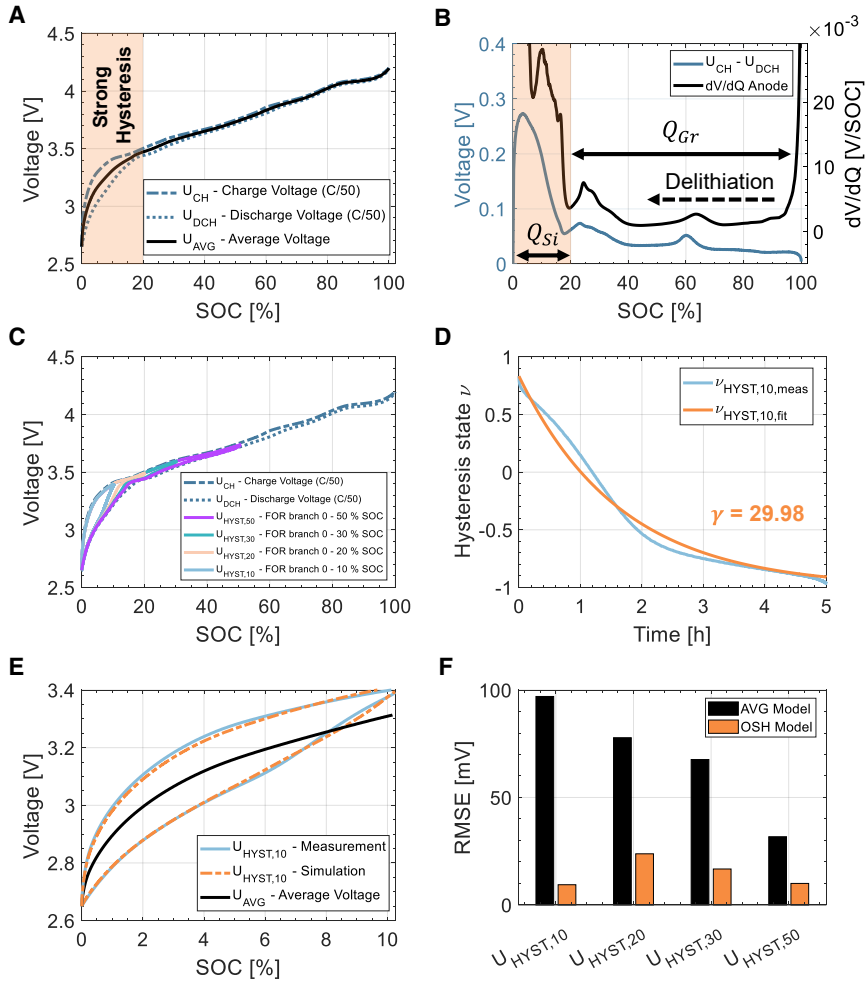

Figure 6. Derivation of a hysteresis model for Gr-SiOx blend anodes

(A) Charge (U_{CH}), discharge (U_{DCH}), and average (U_{AVG}) cell voltage.

(B) Hysteresis voltage difference ($U_{CH} - U_{DCH}$) and anode dV/dQ curve.

(C) FOR branches measured for different partial cycles with cycle depths of 10%, 20%, 30%, and 50%, with starting SOC = 0%.

(D) Calculated and fitted hysteresis state $\nu_{HYST,10}$.

(E) $U_{HYST,10}$ measured and simulated using the implemented OSH model in comparison to using U_{AVG}.

(F) Calculated RMSE error between the measured and simulated voltage for $U_{HYST,10}$, $U_{HYST,20}$, $U_{HYST,30}$, and $U_{HYST,50}$ using the OSH model compared to using U_{AVG}.

inherently higher anode potential of SiOx compared to Gr, SiOx is preferentially lithiated first in lower SOC ranges, up to the initial Gr voltage plateau at ~20% SOC. Above this threshold, competitive lithiation occurs between SiOx and Gr.[70] Conversely, during delithiation, the pronounced hysteresis of SiOx leads to nearly complete delithiation of Gr particles before SiOx particles are delithiated. This results in a clear separation of individual material capacity contributions.[69] Hence, the increased hysteresis voltage in the low-SOC region is attributed to the dominant capacity share of SiOx within this voltage region, similar to the studies of Zilberman et al.[71] and Heugel et al.[72] Considering that the shape of the hysteresis voltage in Figure 6B demonstrates that the average voltage difference in the main working range of the Gr material between 20% and 80% SOC amounts to 36.3 mV, while the average hysteresis voltage in the working range of SiOx between 0% and 20% SOC is significantly higher at 171.7 mV, Figure 6B also depicts the dV/dQ plot for the blend anode during delithiation against the lithium metal counter electrode extracted from the investigated cell. Notably, the peaks in the dV/dQ curve closely correspond to those observed in the hysteresis voltage, suggesting a direct correlation between phase transformations in the anode materials and cell hysteresis.

It becomes clear that neglecting voltage hysteresis for LIBs with SiOx-Gr blend anodes introduces significant potential for errors in later simulations. Hence, to accurately capture the cell-voltage behavior, a hysteresis model is parameterized. The most widely utilized model for incorporating hysteresis effects in LIB models is the one-state hysteresis (OSH) model, as introduced by Plett.[39] This model has been effectively implemented for batteries based on lithium iron phosphate (LFP) as well as batteries with SiOx-Gr blend anodes.[37,38] The OSH model considers the hysteresis state separately from the OCV itself and only describes the behavior of hysteresis between the two main hysteresis branches U_{CH} and U_{DCH}. According to Wycisk et al.,[38] the OCV of the cell U_{OCV} can be described in the OSH model as

$$U_{OCV}(x,t) = U_{AVG}(x) + \frac{U_{\Delta}(x)}{2} \cdot \nu(x,t), \qquad \text{(Equation 5)}$$

with U_{AVG} being the average voltage as per Equation 3 and U_{Δ} the hysteresis voltage as per Equation 4 at a specified SOC x. $\nu(x,t)$ is the hysteresis state, defined between -1 and 1. The differential equation for the hysteresis state can be written as

$$\frac{d\nu(x,t)}{dx} = \gamma(x) \cdot \left(1 - \operatorname{sgn}\left(\frac{dx(t)}{dt}\right) \cdot \nu(x,t)\right), \qquad \text{(Equation 6)}$$

with t being the time, $x(t)$ the SOC, $\gamma(x)$ the SOC-dependent decay rate of the hysteresis transition, and sgn the signum function, taking on 1, 0, or -1 depending on the sign of $\frac{dx(t)}{dt}$. Transforming Equation 6 into the time domain by multiplying both

sides by $\frac{dx}{dt}$ and replacing $\frac{dx}{dt}$ with $\frac{I(t)}{Q_{NOM}}$, with Q_{NOM} being the nominal capacity of the cell, results in

$$\frac{d\nu(x,t)}{dt} = \gamma(x) \cdot \frac{I(t)}{Q_{NOM}} \cdot \left(1 - \operatorname{sgn}\left(\frac{dx(t)}{dt}\right) \cdot \nu(x,t)\right). \quad \text{(Equation 7)}$$

The SOC-dependent model parameter $\gamma(x)$ controls the rate at which the voltage converges to the lower/upper limit of the main hysteresis branch.[73] $\gamma(x)$ is fitted to the measurement data of the first-order reversal (FOR) branches, as introduced in the methods section, by least-squares minimization. In general, it is necessary to measure many of these FOR branches with varying DODs, which makes the overall parameterization very time intensive. However, here our focus will be mainly on the parameterization of $\gamma(x)$ for the lower SOC ranges, as the highest influence of hysteresis is expected within this area, as previously described. Hence, $\gamma(x)$ is individually parameterized for the FOR branches with 10%, 20%, 30%, and 50% DOD, while the same $\gamma(x)$ value is used for all other transitions, based on the fit of $\gamma(x)$ from the FOR branch at 50%. Figure 6C illustrates the FOR branches measured for DODs of 10%, 20%, 30%, and 50%.

Figure 6D depicts the calculated hysteresis state $\nu_{HYST,10,meas}$ for $U_{HYST,10}$. A positive value of ν indicates that the hysteresis transition voltage at this specific point exceeds U_{AVG}, necessitating the scaling and addition of $\frac{U_{\Delta}(x)}{2}$. Conversely, negative values of $\nu_{HYST,10,meas}$ indicate that the transition voltage is below U_{AVG} and that the scaled value of $\frac{U_{\Delta}(x)}{2}$ needs to be subtracted. The corresponding fit to estimate $\gamma(x)$ by solving the differential equation provided in Equation 7 and minimizing the error between $\nu_{HYST,10,meas}$ and $\nu_{HYST,10,fit}$ is also displayed in Figure 6D. The results demonstrate that the decay of the hysteresis state approximates a scaled exponential function effectively.

Figure 6E presents the result of the measured and simulated FOR branch $U_{HYST,10}$. Additionally, U_{AVG} is displayed within that SOC region to illustrate the alternative OCV value utilized in the model when hysteresis effects are not considered. It is evident that the OSH model provides a significantly improved simulation of the voltage behavior, achieving a root-mean-square error (RMSE) of only 9.4 mV. In contrast, the simple usage of U_{AVG}, results in a much higher RMSE of 97.1 mV.

Figure 6F compares the simulation results for various OCV transitions against those obtained by utilizing U_{AVG}. The results clearly demonstrate that the OSH model more accurately captures the hysteresis behavior compared to the use of U_{AVG}. Notably, this improvement is particularly pronounced at low-SOC regions with strong hysteresis.

Assessing the accuracy of the electrical circuit model

The estimated parameters are integrated into an impedance-based coupled thermal-electrical battery simulation framework, the ISEAFrame, developed at our institution (ISEA, RWTH Aachen University) and made publicly available.[74] A comprehensive description of the framework, its components, and the interaction between the electrical and aging model can be found in Rücker et al.,[25] Hust et al.,[75] Barbers et al.,[76] and Hildenbrand et al.[77] The input parameters required for the electrical model, in addition to the fitted ECM parameters, include the power/current profile, the initial cell capacity, and the initial cell SOC. For the thermal model, essential parameters consist of the initial cell temperature, environmental temperature, cell density, heat capacity, and thermal conductivity. The calculated cell density for this specific cell is 2,900 kg/m^3. The specific heat capacity is set to 830 J/kg·K, while the thermal conductivity values are specified as 12 W/m·K in axial direction and 2.4 W/m·K in radial direction, based on measurements conducted on similar cylindrical 18650 NCA cells.[78,79]

The developed model is validated across a broad range of temperatures and SOC levels using current profiles as simulation inputs, derived from previously conducted measurements on the investigated cell. Four distinct types of current profiles are investigated.

(1) Full discharge—temperature variation: A full discharge cycle conducted at a fixed C-rate of C/3 across various temperatures of 5°C, 15°C, 25°C, 35°C, and 45°C.
(2) Full discharge—C-rate variation: A full discharge cycle performed at a fixed temperature of 25°C with varying C-rates of C/2, C/3, C/10, and C/15.
(3) Pulse test: Pulses applied at a constant temperature of 25°C with C-rates of 0.7, 1.0, and 1.3 C in both charge and discharge directions for SOC = 10%, 30%, 50%, 70%, and 90%.
(4) Drive cycle: A current profile extracted from a recorded real-world EV driving cycle scaled down to cell level.

Figure 7A presents the measured and simulated results of a full discharge at a C-rate of C/3 across various temperatures. The duration of the discharge process exhibits a slight decrease at lower temperatures, attributed to reduced available capacity due to higher-occurring overpotentials at lower temperatures. The self-heating of the cell under load is considered by the prior described thermal model. The results indicate that the model effectively approximates the cell behavior across the entire temperature range, with a maximum RMSE of 26.2 mV observed at 5°C. Table S4 summarizes the RMSE and mean absolute percentage error (MAPE) for each simulated scenario. The decrease in model accuracy can be attributed to various changes within the cell that occur at low temperatures, such as diminished ionic conductivity of the electrolyte, lower diffusivity of lithium ions in the electrode lattice according to Arrhenius' law, significant polarization of the anode, and increased charge-transfer resistance at the electrode-electrolyte interface.[80,81] Regarding the latter, modeling the charge-transfer impedance of the anode was omitted, as previously noted, to reduce overall model complexity. Nevertheless, as demonstrated here, the model is sufficient to simulate low-temperature behavior. However, the consideration of anode charge-transfer becomes important when low-temperature performance is critical to the application scenarios of the model. Notably, model accuracy improves at higher temperatures. This enhancement is likely due to the influence of faster

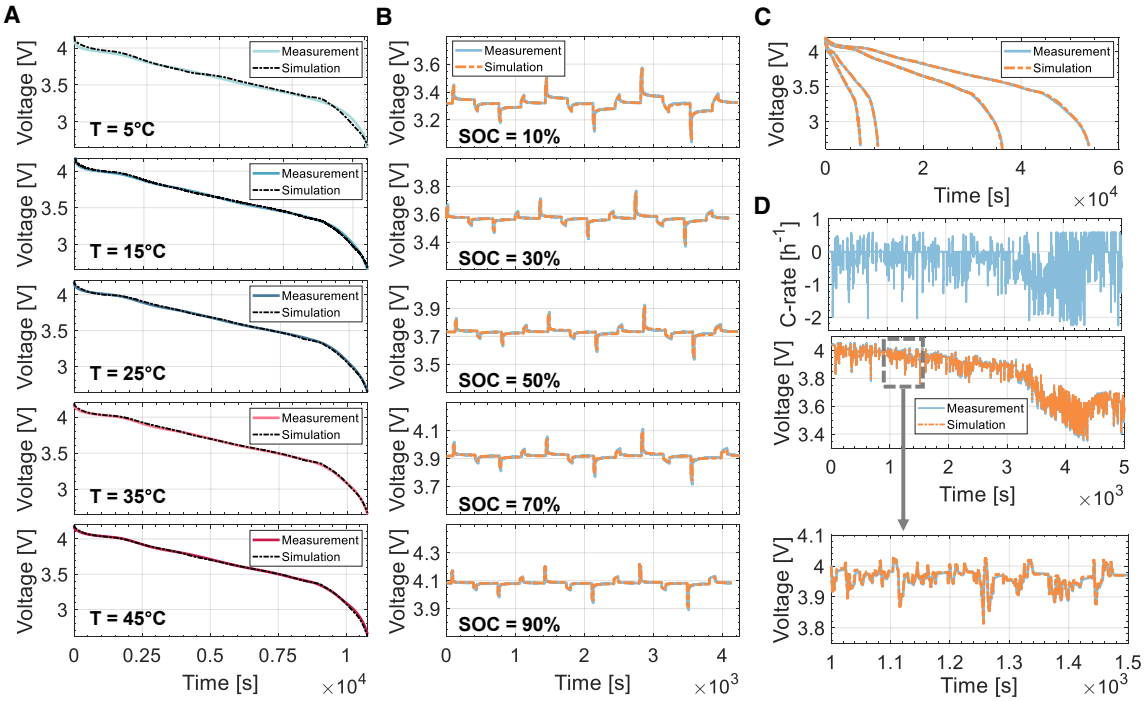

Figure 7. Validation of the ECM for different scenarios

(A) Measured and simulated voltage response of a full discharge at C/3 at different temperatures of 5°C, 15°C, 25°C, 35°C, and 45°C.

(B) Simulated and measured voltage response for pulses at SOCs of 10%, 30%, 50%, 70%, and 90%.

(C) Simulated and measured voltage response of a full discharge at varying C-rates of C/2, C/3, C/10, and C/15.

(D) C-rate and voltage curve for a measured and simulated drive cycle profile, extracted from real-world operation conditions of an EV. The solid lines denote the measured data, while the dashed lines represent the simulated data.

dynamics associated with internal electrochemical processes at elevated temperatures, resulting in decreased polarization contributions and bringing the cell voltage closer to electrochemical equilibrium.[26]

Furthermore, pulses at various SOC levels are simulated to model voltage fluctuations over time. The comparison between the simulated and measured pulse responses is illustrated in Figure 7B for SOC = 10%, 30%, 50%, 70%, and 90%. The model demonstrates strong performance, with RMSE values ranging from 3.5 to 5.1 mV, as summarized in Table S4.

The simulated and measured voltage curves for a full discharge at varying C-rates of C/2, C/3, C/10, and C/15 are depicted in Figure 7C. It becomes visible that the model accurately simulates different polarization contributions across various C-rates. However, as the C-rate increases, the RMSE between the measured and simulated voltage increases, reaching a maximum of 12.3 mV at a C-rate of C/2. Similarly to the influence of temperature on polarization contributions, lower C-rates allow the cell voltage to approach a state closer to electrochemical equilibrium, while higher C-rates increase overpotential contributions to the overall cell voltage.

Additionally, a drive cycle profile is simulated, based on real-world operational conditions of an EV, as presented in Figure 7D. The test cycle consists of driving data for a period of 1.5 h. Further details regarding the test profile used can be found in the methods section. The RMSE between the simulated and measured voltage is 10.2 mV, demonstrating the accuracy of the developed model in predicting real-world operational conditions.

Overall, the model effectively simulates cell dynamics across a wide range of temperatures, C-rates, and SOCs. At lower temperatures, additional non-linearities arise in cell behavior due to slower internal dynamics, which can impact model accuracy and were also observed in other studies.[82] To reduce these inaccuracies, future studies should incorporate the anode charge-transfer impedance, as it significantly affects the overall impedance at low temperatures. Notably, the simulation time for all scenarios remained below 3% of the real time.

Battery aging model development

After validating the electrical model, a semi-empirical aging model is proposed to capture the aging behavior of the given cell under various stress factors. For this purpose, cyclic and calendar aging tests are performed under different stress conditions for the given cell. The test matrices used for the calendar and cyclic aging tests are detailed in the methods section.

The used aging model is a semi-empirical model, analogous to the one presented by Schmalstieg et al.[32] The aging processes that occur during cell storage depend primarily on

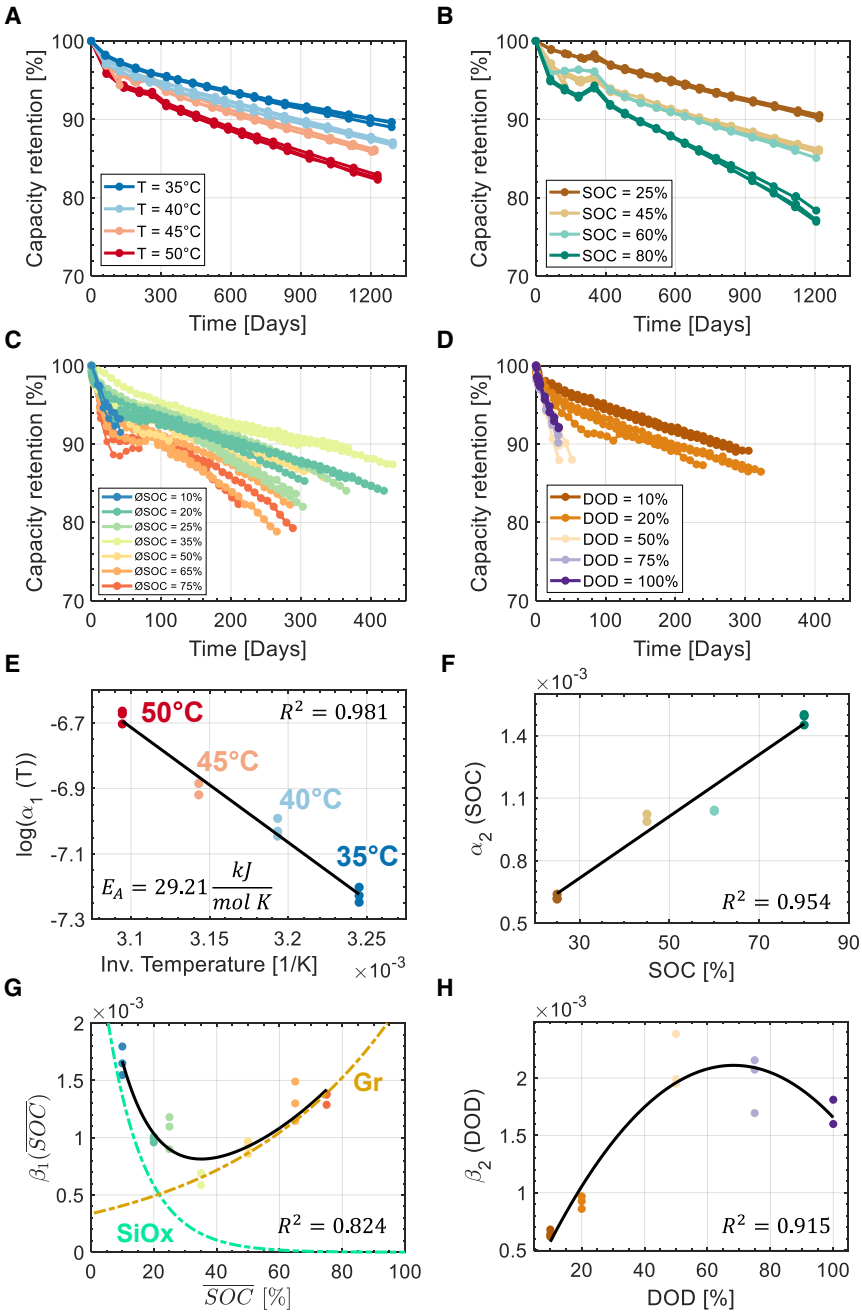

Figure 8. Aging model development

(A) Calendar aging measurements performed at varying storage temperatures at fixed SOC = 45%.

(B) Calendar aging measurements performed at varying storage SOCs at fixed temperature of 45°C.

(C) Cyclic aging measurements performed at varying $\overline{SOC}$s with fixed DOD of 20%.

(D) Cyclic aging measurements performed at varying DODs with fixed $\overline{SOC}$ = 50%.

(E) Arrhenius plot of $\alpha_1(T)$.

(F) Linear fit of $\alpha_2(SOC)$.

(G) Double-exponential fit of $\beta_1(\overline{SOC})$.

(H) Polynomial fit of $\beta_2(DOD)$.

the storage temperature (T), the storage SOC, and the storage duration (t). Figures 8A and 8B depict the capacity progression of the calendar aging results for cells stored at varying ambient temperatures at a fixed SOC of 45% as well as for cells stored at different storage SOCs under a constant ambient temperature of 45°C. Based on the observed cell behavior, the capacity trend of each calendar aging curve is approximated using the following formula:

$$C_{cal}(T, SOC, t) = 1 - \alpha(T, SOC) \cdot t^{0.7}, \quad \text{(Equation 8)}$$

with T being the storage temperature in kelvins, SOC the respective storage SOC in percent, t the storage time in days, $\alpha(T, SOC)$ the aging decay rate, and $C_{cal}(T, SOC, t)$ the normalized cell capacity relative to the initially extracted capacity in the pristine state. Similar approaches have been used with varying exponential constants between 0.5 and 0.75, based on the underlying assumption that the dominant effect during calendar aging is the thickening of the SEI layer, which is inversely proportional to the amount of lithium consumed during storage.[32,34,41]

Figure 8C shows the results of the cyclic aging measurements for cycling around different average SOCs ($\overline{SOC}$) at a fixed DOD of 20%. $\overline{SOC}$ denotes the average SOC around which cycling is performed with a specified DOD. For example, cycling between 80% to 100% in this nomenclature would correspond to a $\overline{SOC}$ = 90% and DOD = 20%. Figure 8D shows the results of cyclic aging for cycling at different DODs around the same $\overline{SOC}$ of 50%. Only data up to a capacity retention of 70% were used to exclude spontaneous cell failures. Similar to Schmalstieg et al.,[32] cyclic aging is assumed to be mainly influenced by DOD, $\overline{SOC}$, and the charge throughput (Q), as given by the equation

$$C_{cyc}(Q, DOD, \overline{SOC}) = 1 - \beta(DOD, \overline{SOC}) \cdot Q^{0.5}, \quad \text{(Equation 9)}$$

with $\overline{SOC}$ being the average cycle SOC in percent, DOD the respective cycle depth in percent, Q the charge throughput in Ah, $\beta(DOD, \overline{SOC})$ the aging decay rate, and $C_{cyc}(Q, DOD, \overline{SOC})$ the normalized cell capacity relative to the initially extracted

capacity in pristine state. The dependency on C-rate is not explicitly addressed in the model. However, it is assumed that higher C-rates primarily result in increased heat generation within the cell.[83] This effect is captured by the thermal model, which will subsequently be factored into the temperature dependency of the overall model, leading to accelerated aging.

$\alpha(T, \mathrm{SOC})$ and $\beta(\mathrm{DOD}, \overline{\mathrm{SOC}})$ describe the decay rates for specific combinations of storage SOC and temperature, respectively DOD and $\overline{\mathrm{SOC}}$. These decay rates are further referred to as aging factors and are obtained by fitting each individual capacity curve to the formulas described in Equations 8 and 9. Subsequently, the values obtained for the aging factors are used to determine the dependency of each individual stress factor (T, SOC, DOD, and $\overline{\mathrm{SOC}}$) on the cumulative aging by establishing a plausible regressive relationship.

It is commonly known that the rate of chemical reaction processes is accelerated at increased temperatures. Hence, the temperature dependency of the aging factors $\alpha(T, \mathrm{SOC})$ is chosen to follow an Arrhenius relationship:

$$\alpha_1(T) = a_1 \cdot e^{-\frac{E_A}{R \cdot T}}, \qquad \text{(Equation 10)}$$

with R being the gas constant and E_A the activation energy. As depicted in Figure 8E, the applicability of the Arrhenius equation is confirmed by the linear dependency of the logarithmic aging factors $\alpha_1(T)$ with $R^2 = 0.981$. This indicates that increased storage temperatures result in exponentially accelerated side reactions, leading to faster capacity loss and aging. The physically interpretable nature of the Arrhenius dependency indicates that it may be extrapolated to temperatures not covered within the calendar aging tests. While this is likely valid for higher temperatures where the primary aging mechanism is expected to remain SEI growth, its applicability for extrapolation to lower temperatures is less certain, as the predominant aging mechanisms in lower-temperature regions might differ from those associated with SEI growth.[43,84,85] In operating scenarios where lower temperatures are critical, lithium plating becomes the primary aging mechanism associated with cyclic aging, rather than calendar aging. In these instances, the traditional Arrhenius dependency represented by a single exponential function might be insufficient and should be expanded to a double-exponential model that captures the increased aging rates at low temperatures.[85] However, when evaluating the impact of storage temperature on calendar aging specifically, the Arrhenius dependency remains applicable. The activation energy can be calculated as $E_A = 29.21$ kJ/mol·K.

The aging factors of the SOC dependency show a linear trend, where higher storage SOCs result in faster aging, as depicted in Figure 8F. Hence, the SOC dependency of the aging factor is approximated using the following equation:

$$\alpha_2(\mathrm{SOC}) = a_2 \cdot \mathrm{SOC} + a_3. \qquad \text{(Equation 11)}$$

The linear fit reproduces the trend of the SOC dependency well, indicated by $R^2 = 0.954$. Higher storage SOCs lead to increased lithiation levels in the anode, causing more significant volume expansion and loss of lithium. However, it should be noted that the lowest measured storage SOC was at 20%, which is still above the SiOx capacity working range. Hence, the purely empirical found linear trend might only be applicable between 20% and 80% SOC.

To account for the overlapping effects of calendar aging during cycling, the capacity loss attributed to solely calendar aging during cycling is estimated using the formula presented in Equation 8. The calculated calendar aging component is subsequently added to the cyclic aging data to isolate the pure cyclic aging component. Although this method has been critically examined in other studies for datasets aimed at identifying distinct degradation modes and linking them to particular aging mechanisms, in our dataset this approach produced satisfactory outcomes in terms of capacity estimation.[86]

As illustrated in Figure 8G, cycling around both high and low $\overline{\mathrm{SOC}}$ levels significantly accelerates the aging rate. This observation is attributed to the fact that cycling at low SOCs primarily utilizes the SiOx content in the anode, leading to substantial deterioration due to pronounced volume expansion. Conversely, cycling at high SOCs induces significant volume expansion of the Gr portion, further contributing to accelerated aging. A double-exponential approach is employed to effectively capture the enhanced aging dynamics of both anode components, as follows:

$$\beta_1(\overline{\mathrm{SOC}}) = b_1 \cdot e^{b_2 \cdot \overline{\mathrm{SOC}}} + b_3 \cdot e^{b_4 \cdot \overline{\mathrm{SOC}}}. \qquad \text{(Equation 12)}$$

The relationship between cyclic aging and DOD is modeled using a quadratic approach, expressed as follows:

$$\beta_2(\mathrm{DOD}) = b_5 \cdot \mathrm{DOD}^2 + b_6 \cdot \mathrm{DOD} + b_7. \qquad \text{(Equation 13)}$$

The results demonstrate that deeper cycles lead to greater aging compared to shallower cycle depths as presented in Figure 8H, which is consistent with findings reported in other studies.[32,87]

The overall combined model expressions for the aging factors associated with calendar and cyclic aging, derived from our previous approximations, are as follows:

$$\alpha(T, \mathrm{SOC}) = (a_1 \cdot \mathrm{SOC} + a_2) \cdot e^{-\frac{K}{T}}, \qquad \text{(Equation 14)}$$

$$\beta(\mathrm{DOD}, \overline{\mathrm{SOC}}) = b_1 \cdot e^{b_2 \cdot \overline{\mathrm{SOC}}} + b_3 \cdot e^{b_4 \cdot \overline{\mathrm{SOC}}} + b_5 \cdot \mathrm{DOD}^2 + b_6 \cdot \mathrm{DOD} + b_7. \qquad \text{(Equation 15)}$$

In the final step, the calendar and cyclic aging factors obtained from the individual fitting of each aging curve are integrated into a three-dimensional fitting algorithm using the dependencies outlined in Equations 14 and 15. This process enables the simultaneous estimation of all model parameters. The estimated parameters from the final fit are summarized in Table S5.

The overall calendar and cyclic capacity loss is therefore given by

$$C(t, Q, T, \mathrm{SOC}, \mathrm{DOD}, \overline{\mathrm{SOC}}) = 1 - \left(\alpha(T, \mathrm{SOC}) \cdot t^{0.7} + \beta(\mathrm{DOD}, \overline{\mathrm{SOC}}) \cdot Q^{0.5}\right). \qquad \text{(Equation 16)}$$

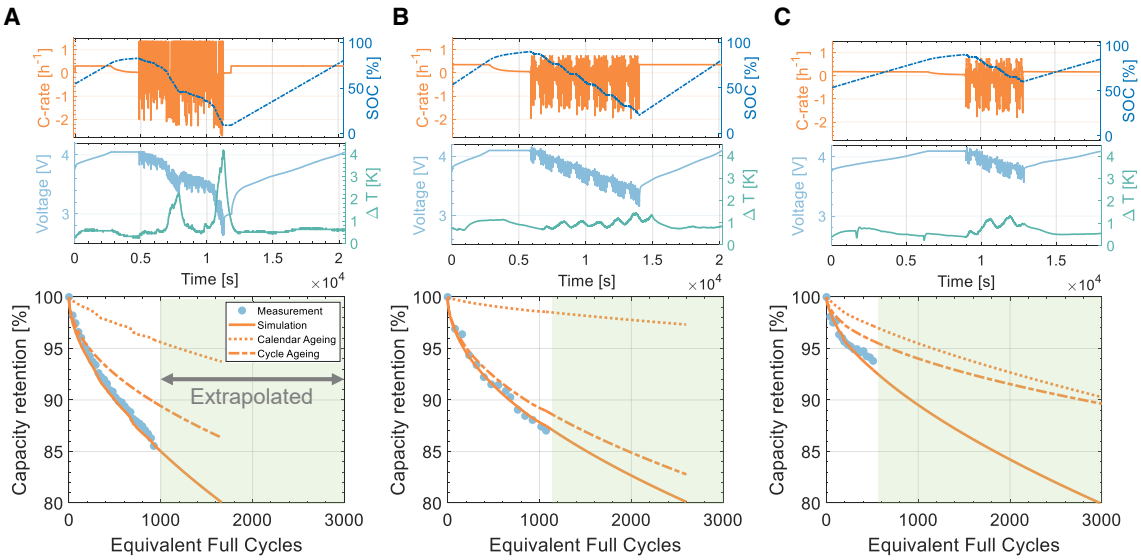

Figure 9. C-rate, SOC, cell voltage, cell heating, and measured/simulated capacity progression for different EV scenarios extracted from real-world operation conditions

(A) Scenario 1: long trip (DOD = 80%, T = 25°C).

(B) Scenario 2: fast charging (DOD = 70%, T = 10°C).

(C) Scenario 3: short trip (DOD = 30%, T = 25°C).

Assessment of aging model accuracy

The developed aging model is validated using aging data obtained from cells cycled under three distinct EV driving scenarios. Figures 9A–9C illustrate, for each scenario, the applied current at the cell level normalized to the nominal capacity, the calculated cell SOC, the cell voltage, the cell heating, and both measured and simulated aging results. In addition, the cyclic and calendar aging components that contribute to overall aging are presented separately to elucidate the dominant aging mechanisms. The simulated results are extrapolated, as indicated by the green-shaded areas, until the overall capacity reaches 80% remaining capacity, which we assume corresponds to the end-of-life (EOL) criteria in our analysis. The RMSE, MAPE, and equivalent full cycles (EFCs) until the EOL criteria is reached are provided in Table S6.

The results indicate that the simulated aging behavior closely approximates the measured aging of the cell. The RMSE between measured and simulated aging ranges from 0.41% to 0.79%, with the maximum deviation remaining below 1% across all aging scenarios. Given that cycling was not conducted under significantly elevated temperatures or exclusively high $\overline{SOC}$s, calendar aging always shows less significant impact on overall aging than cyclic aging for all scenarios tested. Although EVs are typically idle for a substantial portion of their operational time, calendar aging remains critical unless they are stationed in areas with considerably low ambient temperatures. Keil and Jossen[88] demonstrated that, for temperatures up to 25°C, the calendar aging component contributes significantly less to capacity loss compared to cyclic aging. In addition, EV batteries are generally equipped with thermal management systems designed to maintain cell temperature within specified limits.[89] Considering these factors, cyclic aging is expected to predominantly influence the overall aging process, particularly in scenarios involving fast charging or regular usage patterns with deep cycling, as observed in our tests.

Scenario 1 has the highest cycle depth of all scenarios with DOD = 80%, resulting in the largest overall capacity loss reaching 85.5% rest capacity after nearly 1,000 EFCs. The contribution of cyclic aging to the overall capacity loss is twice as much as the calendar aging contribution, thus highlighting the considerable impact of deep cycling on battery aging. Scenario 2 was cycled with a slightly reduced cycle depth of DOD = 70% compared to scenario 1 and at an ambient temperature of 10°C. In comparison to scenario 1, a reduced overall capacity loss of 87.1% rest capacity after nearly 1,150 EFCs, even under fast-charging conditions, is visible. In addition, scenario 2 exhibits the largest disparity between cyclic and calendar aging components. The low amount of calendar aging contribution is primarily attributed to the low ambient test temperature of 10°C, while in comparison to scenario 1 a considerably larger fraction of the overall aging stems from cyclic aging, which is in accordance with various publications.[84,88] Scenario 3 shows the lowest aging gradient among all tested scenarios, offering 93.7% of the initial capacity after 500 EFCs, which is attributed to the low cycle depth of DOD = 30%. In comparison to scenarios 1 and 2, the fraction of calendar aging and cyclic aging on overall aging shows the closest proximity in their respective share of aging. The extrapolated trends of the simulated results suggests that upon reaching the EOL criteria at 80% remaining capacity, the shares of calendar and cyclic aging influence overall aging to a similar extent for scenario 3. This indicates that indeed for short trips with no fast-charging requirements or deep cycling, calendar aging has a pronounced influence on the overall aging, while cyclic aging is drastically reduced. The model performance for

this specific scenario exhibits the highest overall error. This increased error can be attributed to the limitations of the available cyclic aging data, which were used to parameterize the model. As shown in Figure 8G, no measurements were conducted for DODs between 20% and 50%. Instead, within this range, the DOD dependency is solely interpolated between the two nearest available measurements at 20% and 50%. This suggests that the DOD dependency within the cyclic aging component is slightly overestimated, resulting in an overall overestimation of aging for this scenario.

The estimated results obtained from the aging model are particularly interesting, considering that the validation data were derived from cycling the cell at ambient temperatures of 25°C and 10°C, which are significantly lower than the temperatures used to parameterize the temperature dependency in the aging model. This suggests that extrapolation based on the Arrhenius equation is a valid approach. However, it is important to note that the relatively minor influence of calendar aging at low temperatures may have contributed to maintaining confidence in this assumption, as any discrepancies arising from extrapolating the model in scenarios where it does not accurately reflect aging effects are likely to be negligible. Although the model was fitted on aging data from synthetic load cycles, it yields reasonable results for highly dynamic and diverse automotive load cases. Similar to Schmalstieg et al.[32] and Sarasketa-Zabala et al.,[33] our findings indicate that extrapolating models based on accelerated measurements to non-accelerated standard operating conditions is a feasible approach. Nonetheless, it is important to recognize certain limitations of the model. In particular, the model does not consider the relaxation behavior of LIBs, which has been demonstrated to significantly promote capacity recovery effects.[77,90,91] This effect is particularly pronounced following accelerated aging conditions, such as elevated C-rates, which lead to increased inhomogeneity in lithium distribution within the negative electrode.[92,93] As this relaxation behavior is not appropriately covered in either accelerated cyclic aging tests or validation measurements, cell aging may inadvertently be exacerbated. Hence, the results should be viewed as worst-case approximations, which remain valuable for manufacturers when considering warranty commitments.[90,94] Additionally, factors such as spontaneous cell failure and statistical uncertainties associated with fitted model parameters and the resulting aging estimations have not been addressed but will be investigated in our future work. Furthermore, for scenarios beyond the regular operation of the cell in EV or ESS scenarios, extrapolating the obtained model to extreme conditions such as ultra-high temperatures or C-rates, may not be feasible.

Despite these limitations, the qualitative trends of the respective aging trajectories are simulated with good agreement. The simulated aging rates for different load scenarios align well with actual measured aging rates in descending order: scenario 1 > scenario 2 > scenario 3. Similarly, the attainment of the EOL criteria, as presented in Table S6, shows a consistent trend, with scenario 1 reaching the EOL criteria the fastest at 1,664 EFCs, followed by scenario 2 at 2,598 EFCs and scenario 3 at 3,097 EFCs. Consequently, it appears more reasonable to evaluate impedance-based aging models by their capability to provide qualitative comparisons across different operating strategies. This enables identification of trends and patterns in the behavior of LIBs under varying conditions and can help manufacturers to identify specific optimization opportunities within a battery pack. Moreover, understanding the varying influences of calendar and cyclic aging components can help identify specific optimization opportunities within a battery pack while serving as an early-warning system for potential issues as performance deviates from expected trends. Consequently, the model can be considered as an overall viable tool for estimating the impact of aging under various real-world operational conditions for EVs.

Accelerating aging model acquisition

The dataset utilized to parameterize the aging model was collected over several years and involved numerous cells tested under various conditions. Although extended test periods are essential for comprehensively understanding cell internal degradation processes for later electrochemical analyses, shorter test durations are preferable for modeling purposes. Consequently, accelerating model acquisition by minimizing test time and altering test conditions becomes crucial. Therefore, a sensitivity analysis is performed on all model parameters to evaluate the impact of modifications to these parameters on the model output. Following this analysis, the aging model is refitted using fractional portions of the total available calendar and cyclic aging data, aiming to identify the shortest test duration necessary to achieve acceptable model outcomes. The same model structure as outlined in the previous section is employed throughout this section.

Revealing key stress factors through sensitivity analysis

A global sensitivity analysis is performed as described in the methods section. Figure 10A presents the calculated absolute rank correlation coefficients for the calendar aging model parameters a_1, a_2, and K in relation to the model output across varying storage SOCs and temperatures. It becomes evident that, under different storage conditions, the overall correlation with the model output remains consistent across all model parameters. Generally, the temperature parameter K governs the overall output of the model at any investigated storage SOC and temperature, as indicated by the high correlation with the model output. In contrast, varying the storage SOC parameters a_1 and a_2 shows no significant correlation with their corresponding generated model output. Thus, the order of significance for the parameters in the calendar aging model can be classified as follows: $K > a_1 > a_2$. The results can be interpreted for physical plausibility and their implications for a reduced testing strategy. Specifically, it appears that for calendar aging, temperature during storage has a greater influence on the model output than storage SOC, which aligns with expectations based on the exponential nature of the Arrhenius' law, rendering the temperature dependency superior. Importantly, this finding does not introduce any bias into the sensitivity analysis, since only monotonic relationships are evaluated using the Spearman rank correlation coefficient. This ensures a robust assessment of parameter influences while accounting for the inherent characteristics of the underlying relationships in the model. Thus, for this specific cell chemistry, more emphasis should be placed on temperature variations in calendar aging studies. It is recommended

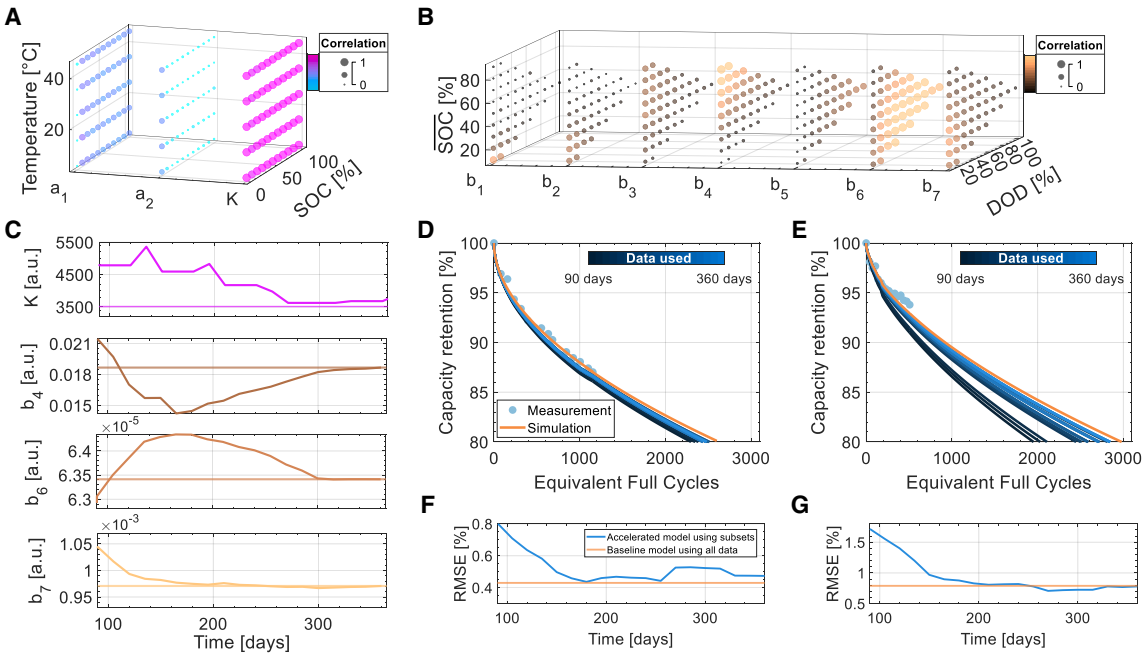

Figure 10. Investigating the impact of reduced test duration on model accuracy

(A) Absolute rank correlation coefficients for the calendar aging model parameters a_1,a_2, and K at varying storage SOCs and temperatures.

(B) Absolute rank correlation coefficients for the cyclic aging model parameters b_1–b_7 under varying operating conditions.

(C) Progression of successively fitted parameters using only subsets of the entire available dataset, with up to 360 days of data for sensitive parameters K,b_4,b_6, and b_7.

(D and E) Simulation of (D) scenario 2 and (E) scenario 3 using different fractional portions of the available dataset between 90 and 360 days. The orange solid line represents the simulation results obtained using the entire dataset.

(F and G) Average RMSE for (F) scenario 2 and (G) scenario 3 between the simulated and measured capacity curve for different fractional portions of the available dataset between 90 and 360 days.

that variations in storage SOC during calendar aging tests be implemented sparingly. The validation of the aging model demonstrated that extrapolating the fitted Arrhenius dependency from accelerated aging tests at elevated storage temperatures (35°C–50°C) to lower ambient temperatures (10°C) to estimate the impact of calendar aging seems feasible, thereby facilitating accelerated data aggregation.

Figure 10B illustrates the absolute values of rank correlation coefficients for the cyclic aging model parameters b_1–b_7 under varying operating conditions. The sensitivity analysis reveals that parameter b_6 exhibits a high correlation with the model output across different operating windows. Parameters b_1 and b_2 demonstrate stronger correlation with the model output in lower-$\overline{SOC}$ regions, while b_3 and b_4 show increased correlations at higher-$\overline{SOC}$ regions. This behavior can be attributed to different material components of the anode, specifically SiOx and Gr, that influence the output of the aging model in their respective cycling windows. Hence, the proposed $\overline{SOC}$ dependency using two exponential functions effectively captures the differing cycling effects in areas where SiOx or Gr predominately contributes to the overall capacity. Regarding parameter variations associated with DOD, it is evident that changes in parameter b_6 yield the strongest correlation with the model output over a wide DOD range, while parameter b_7 exhibits high correlation primarily at low DODs in combination with low $\overline{SOC}$s. The cyclic aging parameters indicate that the model output is sensitive to both embedded dependencies $\overline{SOC}$ and DOD. In the cyclic aging model, the parameters can be ranked in significance as follows: $b_6 > b_4 > b_7 > b_5 > b_3 > b_1 > b_2$. Consequently, incorporating both stress factors is crucial for accurate lifetime estimation. However, given that the DOD dependency demonstrates a stronger correlation with the model output across a broader operating range, it is recommended that priority should be given to the DOD dependency over the $\overline{SOC}$ dependency. The pronounced influence of DOD on cyclic aging aligns with the findings reported by Wildfeuer et al.[95]

Examining the impact of test time reduction on model accuracy

To investigate the influence of reduced test duration on model precision, fractional portions of the total dataset are collected at specific test intervals ranging from 90 days to 360 days, with increments of 15 days. For each of these 19 subsets, the previously described aging model is refitted, aiming to provide insights into how reduced data availability from shorter testing durations impacts model performance and alters the estimated model parameters.

The progression of model parameters that exhibit a strong correlation with the model output is analyzed based on the previously conducted sensitivity analysis. Figure 10C illustrates the

evolution of the parameters K, b_4, b_6, and b_7 following successive refitting of the aging model using 19 distinct subsets. The straight line represents the fitted value for each respective parameter derived from the complete dataset. It is evident that the parameter values obtained from the subsets demonstrate a converging trend toward those derived from the entire dataset. Notably, the calendar aging parameter K shows no significant change in its value beyond 270 days, suggesting that a testing duration of 270 days would suffice from a modeling perspective. This finding indicates a substantial potential for test time reduction compared to the actual performed calendar aging test dataset, which spans over 1,200 days. Regarding cyclic aging parameters, both b_4 and b_6 closely align with their corresponding values obtained from the complete dataset after approximately 300 days of testing. In contrast, parameter b_7 exhibits no significant deviation from its value derived from the complete dataset after just 170 days.

To evaluate the accuracy of the models derived from different subsets, we conducted simulations for scenarios 2 and 3, as illustrated in Figures 10D and 10E. The results clearly demonstrate that as testing duration and, thus, data availability increases, the accuracy of the model also improves. The average RMSE between the simulated and measured capacity curves for various subsets, utilizing data ranging from 90 to 360 days, is presented in Figures 10F and 10G. For scenario 2, the RMSE decreases from an initial value of 0.8% to 0.47%, indicating a modest reduction with increasing data availability. Notably, even with just 90 days of data, estimation errors below 1% are achieved, while approximately 150 days of data suffices to attain similar estimation errors as those derived from the complete dataset (0.42%). The low estimation errors observed, even with limited data availability, can be attributed to the minimal impact of calendar aging in scenario 2 due to the environmental test temperature of 10°C. Consequently, although the temperature parameter K that governs calendar aging converges after approximately 270 days, an over- or underestimation to a certain degree within this period does not have a significant impact on the overall model error. In this case, cyclic aging emerges as the dominant factor that necessitates less testing time to accurately represent long-term aging trajectories compared to calendar aging. Furthermore, the variation among the different model estimations for reaching the EOL cycle is minimal, with values ranging from 2,291 to 2,507 EFCs, depending on the amount of data used. This suggests that, for this scenario, even a testing duration of 90 days would have been sufficient for a quantitative aging estimation.

In scenario 3, the variation in reaching the EOL criteria from the model estimations derived from different subsets is more pronounced, ranging between 1,950 and 2,843 EFCs. The RMSE decreases from an initial value of 1.8% for the subset considering only 90 days of data to 0.78% for the subset incorporating 360 days of available data. The most substantial reduction in RMSE occurs within the first 200 days. The results generally demonstrate a trend similar to that observed in scenario 2. As testing duration increases, the accuracy of the simulations improves significantly. However, due to substantial variations in the estimated results from different subsets, a testing duration of 90 days is inadequate for accurately predicting the aging trajectory in this specific scenario. This limitation can be primarily attributed to the increased impact of calendar aging in this scenario, which exerts a greater influence on overall aging compared to scenario 2. These findings indicate that different operational scenarios can significantly impact the amount of testing required to obtain acceptable model results.

In summary, we presented the development, parameterization, and validation of a semi-empirical aging model coupled with a thermal-electrical impedance model for a commercially available NCA LIB featuring a SiOx-Gr blend anode. The integration of results obtained from DRT analysis, EIS, and pulse measurements within the model allowed an accurate characterization of the complex electrical behavior of the battery under various operational conditions. By incorporating a hysteresis model, the significant volume expansion effects associated with silicon during lithiation and delithiation were effectively accounted for. The presented aging model captures both calendar and cyclic aging mechanisms, yielding predictions of capacity loss that align closely with accelerated real-world operational scenarios, achieving less than 1% deviation from validation measurements. The presented detailed instructions on how to develop the impedance-based aging model can be used as a guideline for others who wish to create a similar impedance-based aging model. Additionally, we offer the following recommendations.

A sensitivity analysis evaluated the impact of each aging model parameter on the model output, followed by refitting the model with fractional portions of available calendar and cyclic aging data between 90 and 360 days, aiming to identify the shortest test duration necessary to achieve acceptable model outcomes. The findings suggest that testing conditions can strategically be optimized alongside shorter testing durations while still attaining satisfactory levels of model accuracy, depending on the specific application of the aging model. Based on these findings, we offer the following recommendations.

Accelerating model development: Embracing open-source resources

Creating an impedance-based model from scratch is a challenging task, with measurements alone often taking several months. Developing the entire tool chain required for constructing the model can take even longer. However, utilizing available open-source tools can significantly reduce the time needed to obtain the model. Furthermore, when researchers use the same tools, results become more comparable and integrable across studies. Additionally, these tools can be extended by the community, benefiting all users. Therefore, we recommend adhering to already published tools in this area, similar to those employed in our study here. The presented aging model along with all relevant data are publicly accessible for use by industry and research institutions.

Enhancing ECM accuracy through advanced techniques and hysteresis modeling

The developed ECM successfully simulates battery dynamics across a range of temperatures and SOCs. Researchers should consider the use of DRT as a valuable tool for establishing reasonable model assumptions. Improved results can be achieved by differentiating between fast and slow battery dynamics through the integration of both EIS and pulse

measurements. For enhanced accuracy, particularly at low temperatures, incorporating the polarization of the anode charge-transfer impedance is recommended. Additionally, for LIBs with silicon fractions in the anode, implementing a hysteresis model, albeit in a minimized form as demonstrated in our study, is essential to accurately capture real cell voltage.

Optimizing test conditions for modeling purposes by prioritizing key stress factors

The sensitivity analysis carried out has identified key stress factors and highlighted the importance of understanding the dynamics of individual model parameters over different test durations to effectively accelerate model acquisition. There is substantial potential to reduce test efforts while ensuring reliable model performance by prioritizing key stress factors such as temperature for calendar aging and DOD for cyclic aging.

Based on the results obtained, we recommend conducting accelerated calendar aging tests at a minimum of four relevant temperature levels, specifically at elevated storage temperatures above 30°C, as the extrapolation of the Arrhenius' law to lower temperatures proved to be a feasible approach due to the smaller impact of calendar aging on the overall aging at low storage temperatures. It is recommended that variations in storage SOC during calendar aging tests be implemented more sparingly.

For cyclic aging tests, it is essential to incorporate both investigated stress factors $\overline{\text{SOC}}$ and DOD for an accurate lifetime estimation. However, since the DOD dependency showed stronger correlation with model output across a broader operating range, priority should be given to DOD dependency over $\overline{\text{SOC}}$ dependency. It is recommended to perform cyclic aging tests considering at least five different DODs within the relevant operation range. Meanwhile, the $\overline{\text{SOC}}$ dependency should be considered more conservatively with a maximum of three test points, while especially for cells with silicon content the $\overline{\text{SOC}}$ ranges between 5% and 20% should be investigated, as the impact on model output has demonstrated a strong correlation within these intervals.

Reducing test time by defining operational ranges of the aging model

The findings demonstrate that different operational scenarios can significantly influence the amount of testing necessary to achieve acceptable model results. In our case, scenario 2 yielded satisfactory outcomes with just 90 days of data (RMSE = 0.8%), while scenario 3 showed considerable variations when the data used for model fitting was reduced to fewer than 200 days. Therefore, it is crucial to clearly define the operational ranges for which the aging model is intended to predict performance. Additionally, the results indicate that required test durations vary based on the relative influence of calendar and cyclic aging within the simulated operating scenarios. Extended test periods are particularly essential for accurate modeling of calendar aging. In situations where calendar aging is expected to have minimal impact, such as in cold-weather regions or in applications involving only fast charging, satisfactory model results can be achieved with only 90 days of testing. Conversely, in scenarios where calendar aging is not significantly overshadowed by cyclic aging, it is advisable to conduct at least 200 days of aging to secure satisfactory model outcomes.

It is important to note that these recommendations are primarily focused on the modeling aspect. For more comprehensive electrochemical analyses, longer test durations and examination of additional stress factors may be necessary. Furthermore, the results should be viewed as worst-case approximations, since all tests were conducted under constant-stress conditions without substantial relaxation phases. Future research should aim to explore the interactions of various additional stress factors, such as resting periods on cyclic aging. Nevertheless, the provided recommendations can serve as a foundation for establishing testing requirements aimed at ultimately developing aging models based on obtained data.

Overall, this research contributes to the understanding of modeling LIBs with SiOx-Gr blends. The open-source toolchain and datasets presented will facilitate further investigations into battery performance prediction across various applications such as EVs or ESSs.

METHODS

Investigated cell

In this work, commercially available high-energy cylindrical Samsung SDI INR18650 35E LIBs are investigated. The nominal capacity is specified by the manufacturer as 3.35 Ah, and the voltage limits are given as between 2.65 and 4.2 V. The electrode material consists of a blend of Gr + 1.5 wt % SiOx on the anode and NCA as the cathode material. More detailed cell specifications can be found in Kuntz et al.[96] All measurements presented were conducted in accordance with the specifications outlined by the manufacturer and can be found in Morales Torricos et al.[93,97] and Willenberg et al.[93,97]

Electrochemical impedance spectroscopy and pulse measurements

All EIS measurements were performed using a Digatron EIS-meter within a Binder MK53 climate chamber in which the chosen test temperature is adjusted and controlled with an accuracy of ±1 K.

EIS and pulse measurements were performed for five different temperature levels (5°C, 15°C, 25°C, 35°C, and 45°C) at 11 equidistant SOCs between 100% and 0%. The decision to restrict the model to these temperature limits is based on the manufacturer's data sheet, which indicates that the cell should not be charged at temperatures exceeding 45°C. The cell was allowed to rest for 12 h at the respective testing temperature. Before starting the EIS and pulse characterization routine, the cell is fully charged until the upper cutoff voltage is reached with $C/3$ in constant-current (CC) constant-voltage (CV) mode until the float current falls below $C/50$ (68 mA). Following a 15-min resting phase, a low-current measurement with $C/15$ in discharge and charge direction is performed between the respective cutoff voltages. Thereafter, a capacity test at $C/3$ in discharge and charge direction is performed. After the final CCCV charging phase of the capacity test, starting in fully charged state (that is, SOC = 100%), impedance spectra were recorded with the AC amplitude of the applied signal perturbation at 10 mV and an applied current of less than 2 A. Each EIS measurement was performed in a frequency range from 6 kHz to 10 mHz with eight frequencies per

decade, resulting in a total of 48 measured frequencies. After the initial measurement, the targeted SOCs were adjusted in ascending order Ah-based using the prior obtained C/ 3 discharge capacity from the capacity test performed at the respective temperature level with a C-rate of C/3. Thereafter, a rest period is employed for as long as until the voltage fluctuation falls below 5 mV or a maximum of 3 h has passed after reaching each targeted SOC.

After measuring the impedance spectra, pulse measurements are performed at the respective SOC and temperature. For this purpose, pulses with a C-rate of 0.7 C, 1 C, and 1.4 C were successively applied in charge and discharge direction with a duration of 20 s. To compensate for the additional charge throughput after each charge/discharge pulse, the charged/discharged amount of capacity is withdrawn/added before performing the next pulse measurement using a $C/3$ discharge/charge.

Distribution of relaxation times

The DRT enables a deconvolution of the impedance spectra and was originally introduced to evaluate impedance measurements of solid oxide fuels, while in recent years it has also been widely used to analyze impedance spectra of LIBs.[52,53,55,98] The main advantage compared to conventional analysis methods, such as fitting an ECM, is that no *a priori* choice of circuit elements is necessary, thereby increasing the physical interpretability of the impedance data. This is achieved mathematically by transforming the measured impedance data from the frequency domain into the time domain using a distribution function of relaxation times with corresponding relaxation amplitudes, expressed as

$$Z(f) = R_0 + \int_0^{\infty} \frac{g(\tau)}{1+i2\pi f\tau} d\tau, \qquad \text{(Equation 17)}$$

where R_0 describes the ohmic resistance, and $g(\tau)$ is a suitable function describing the relaxation time characteristics of the measured electrochemical system, paired with their respective resistive contribution.[99,100] Every physical process occurring within the battery results in a peak in the DRT with associated center frequency indicating the rate of the polarization, whereas the magnitude provides insights into the impedance contributions of different processes to the overall impedance of the LIB.

Since impedance measurements are typically acquired with a certain number of points per decade, Equation 17 can be conveniently rewritten in logarithmic form by substituting $\tau = \exp^{\ln(\tau)}$. Applying the DRT necessitates that the impedance of the measured system meets several converging constraints.[101] Usually these constraints are not fulfilled for LIBs due to the inductive behavior at HF and the capacitive behavior at LF. Hence, the impedance function in Equation 18 is extended by the transfer function of an inductance to account for the HF effect. As no quantitative statements regarding the diffusive part will be drawn from the LF DRT portion, no compensation of the capacitive effects is required. Furthermore, the integral is normalized, resulting in the separation from the polarization resistance R_{pol}, ultimately yielding to

$$Z(f) = R_0 + i2\pi fL + R_{pol} \cdot \underbrace{\int_{-\infty}^{\infty} \frac{\tilde{\gamma}(\ln(\tau))}{1+i2\pi f\tau} d\ln(\tau)}_{=1}, \qquad \text{(Equation 18)}$$

with $\gamma(\ln(\tau)) = R_{pol} \cdot \tilde{\gamma}(\ln(\tau))$.

A more comprehensive review and mathematical description of the DRT can be found in Plank et al.[102] The presented DRT within this paper is mainly utilized to deconvolute different processes at IF and is calculated using the open-source-available DRTtools.[99,100] To ensure reliable DRT calculation, the required parameters to calculate the DRT are identical for each EIS measurement.

Hysteresis characterization measurements

The hysteresis characterization measurements were performed using a Neware BTS-4008-5V6A circuit within a Binder MK240 climate chamber, where the selected test temperature of 25°C is adjusted and controlled with an accuracy of ±1 K. The cell was allowed to rest for 12 h at the respective testing temperature. The cell was preconditioned by fully discharging it to the lower cutoff voltage using a CCCV discharge with a C-rate of C/3 until the float current was below C/50. Following a 15-min resting phase, the cell was discharged again at C/50 to ensure it was completely discharged.

Initially, a complete charge-and-discharge cycle was performed to obtain the main hysteresis branch that bounds the hysteresis model. For all measurements of the relevant hysteresis curves, a C-rate of C/50 was used to minimize polarization effects. Additionally, after each discharge procedure, a resting phase of 15 min was used before conducting another discharge with C/50 to the lower cutoff voltage to ensure that the cell was fully discharged. To assess transition behavior during partial charge/discharge cycles, FOR branches were measured, as defined in Plett.[39] After a complete discharge, a specific SOC was targeted Ah-based using the prior measured C/50 discharge capacity. The cell was then discharged again to the lower cutoff voltage. This procedure was repeated for different SOC levels ranging from 10% to 50% in increments of $\Delta SOC = 10\%$.

Calendar and cyclic aging measurements

The calendar aging tests to fit the aging model were performed at our institute (ISEA, RWTH Aachen University) under variation of ambient temperature and SOC. Four different ambient temperatures of 35°C, 40°C, 45°C, and 50°C were investigated. Furthermore, four different SOCs at 25%, 45%, 59%, and 80% were selected to investigate the influence of different lithiation states on calendar aging. An in-depth analysis of these calendar aging measurements and procedures used can be found in the work of Frie et al.[103]

The aging measurements used to fit the cyclic aging model were also performed at our institute (ISEA, RWTH Aachen University) for five different DODs and eight varying average SOCs. The C-rate employed for all cyclic aging measurements was 0.5 C during the charging phase, followed by an Ah-based discharge corresponding to the investigated DOD. An in-depth

analysis and description of the performed cyclic aging tests can be found in the works by Willenberg et al.[97,104,105]

The test matrices used to fit the calendar and cyclic aging model are presented in Tables S7 and S8. Multiple cells were used for the same operating point in order to show the reproducibility of the measurements.

Validation profiles

Several automotive load cases serve for model validation. For this purpose, dynamic load profiles were measured and scaled down to cell level, as described in Schreiber et al.,[94] Wassiliadis et al.,[106] and Jöst et al.[107] For a higher degree of realism, power profiles are applied to the cells, such as in the vehicle. Discharging is terminated after extracting a predefined amount of charge, representing constant range requirements throughout the experiment. Two long-distance scenarios with 80% DOD (scenario 1) and 70% DOD (scenario 2) and one shorter trip with 30% DOD (scenario 3) are used. The cells are charged to 4.1 V or 90% SOC, respectively, using different charging strategies. Scenario 1 uses a CCCV charging protocol with 1.02 A. Scenario 2 applies a CCCV charging strategy with 1.2 A, which is the maximum continuous charging current defined by the cell manufacturer, simulating a fast charging event. Scenario 3 uses a constant-power constant-voltage (CPCV) protocol, simulating an 11 kW wallbox charging event, which yields a charging power of 2.32 W on cell level. The test specifications are summarized in Table S9.

A reference performance test (RPT) is carried out on a regular basis following the presented RPT routines in Schreiber et al.[94] and Jöst et al.[107] Both cycling and RPT are performed at 25°C ambient temperature. Only for scenario 2, the cell is cycled at 10°C ambient temperature.

Sensitivity analysis

Each parameter of the semi-empirical aging model affects the accuracy of the model output to varying degrees. Hence, a sensitivity analysis considering different operation points was carried out in this work to investigate the sensitivity of the calendar and cyclic aging model parameters under varying operating/storage conditions. To examine the full range of possible outcomes a global sensitivity analysis is conducted, in which all variables are simultaneously varied by logarithmically covering latin hypercube sampling.[108] The simulations were performed in MATLAB using lhsdesign, with 1,000 simulations executed for each operation point. Each parameter of interest in the calendar and cyclic aging model was correlated with the change in the respective aging factor at varying operating ranges using Spearman's rank correlation coefficient.[109] Table S10 displays the ranges of parameters utilized.

RESOURCE AVAILABILITY

Lead contact

Requests for further information and resources should be directed to and will be fulfilled by the lead contact, Ahmed Chahbaz (ahmed.chahbaz@isea.rwth-aachen.de).

Materials availability

No newly generated materials were presented within this paper.

Data and code availability

- The newly generated data featured in this study can be accessed in the RWTH University repository (https://doi.org/10.18154/RWTH-2025-04811).
- The modified code for the open-source simulation tool ISEAFrame, which includes the impedance-based aging model presented in this study, is available in the RWTH University GIT repository (https://git.rwth-aachen.de/isea/framework/-/tree/Publication_Samsung_35E_-Model).
- Any additional information required to reanalyze the data reported in this paper is available from the lead contact upon request.

ACKNOWLEDGMENTS

This work was funded by the Federal Ministry of Education and Research via grant BMBF 03XP0320A.

AUTHOR CONTRIBUTIONS

A.C. drafted the manuscript, conducted experiments, and analyzed and interpreted data. M.S. and J.M.H. contributed to data generation and analyzed data. J.R. contributed to model development. G.S., D.U.S., and M.L. supervised the research and provided oversight of the work.

DECLARATION OF INTERESTS

The authors declare that they have no known competing financial interests or personal relationships that could have appeared to influence the work reported in this paper.

DECLARATION OF GENERATIVE AI AND AI-ASSISTED TECHNOLOGIES

During the preparation of the manuscript, the authors used GPT4/OpenAI to improve readability and language, as they are non-native English speakers. After using this tool, the authors reviewed and edited the content as needed and take full responsibility for the content of the publication.

SUPPLEMENTAL INFORMATION

Supplemental information can be found online at https://doi.org/10.1016/j.xcrp.2025.102654.

Received: February 25, 2025
Revised: April 21, 2025
Accepted: May 21, 2025
Published: June 12, 2025

REFERENCES

1. Brückmann, G., Willibald, F., and Blanco, V. (2021). Battery electric vehicle adoption in regions without strong policies. Transport. Res. Transport Environ. *90*, 102615.
2. Chen, H., Chahbaz, A., Yang, S., Zhang, W., Sauer, D.U., and Li, W. (2024). Thermodynamic and kinetic degradation of LTO batteries: Impact of different soc intervals and discharge voltages in electric train applications. eTransportation *21*, 100340.
3. Zhao, C., Andersen, P.B., Trætholt, C., and Hashemi, S. (2023). Grid-connected battery energy storage system: a review on application and integration. Renew. Sustain. Energy Rev. *182*, 113400.
4. Turcheniuk, K., Bondarev, D., Amatucci, G.G., and Yushin, G. (2021). Battery materials for low-cost electric transportation. Mater. Today *42*, 57–72.
5. Barré, A., Deguilhem, B., Grolleau, S., Gérard, M., Suard, F., and Riu, D. (2013). A review on lithium-ion battery ageing mechanisms and estimations for automotive applications. J. Power Sources *241*, 680–689.

6. Schmalstieg, J., Rahe, C., Ecker, M., and Sauer, D.U. (2018). Full cell parameterization of a high-power lithium-ion battery for a physico-chemical model: Part I. Physical and electrochemical parameters. J. Electrochem. Soc. *165*, A3799–A3810.

7. Ecker, M., Tran, T.K.D., Dechent, P., Käbitz, S., Warnecke, A., and Sauer, D.U. (2015). Parameterization of a physico-chemical model of a lithium-ion battery: I. determination of parameters. J. Electrochem. Soc. *162*, A1836–A1848.

8. Finegan, D.P., Zhu, J., Feng, X., Keyser, M., Ulmefors, M., Li, W., Bazant, M.Z., and Cooper, S.J. (2021). The application of data-driven methods and physics-based learning for improving battery safety. Joule *5*, 316–329.

9. Liu, K., Ashwin, T.r., Hu, X., Lucu, M., and Widanage, W.D. (2020). An evaluation study of different modelling techniques for calendar ageing prediction of lithium-ion batteries. Renew. Sustain. Energy Rev. *131*, 110017.

10. Wang, Z., Shi, D., Zhao, J., Chu, Z., Guo, D., Eze, C., Qu, X., Lian, Y., and Burke, A.F. (2024). Battery health diagnostics: Bridging the gap between academia and industry. eTransportation *19*, 100309.

11. Wang, X., Wei, X., Zhu, J., Dai, H., Zheng, Y., Xu, X., and Chen, Q. (2021). A review of modeling, acquisition, and application of lithium-ion battery impedance for onboard battery management. ETransportation *7*, 100093.

12. He, R., He, Y., Xie, W., Guo, B., and Yang, S. (2023). Comparative analysis for commercial Li-ion batteries degradation using the distribution of relaxation time method based on electrochemical impedance spectroscopy. Energy (Calg.) *263*, 125972.

13. Huang, R., Wang, X., Jiang, B., Chen, S., Zhang, G., Zhu, J., Wei, X., and Dai, H. (2023). Revealing the electrochemical impedance characteristics of lithium-ion battery (nickel-cobalt-aluminum vs. graphite) under various alternating current amplitudes. J. Power Sources *566*, 232929.

14. Ecker, M., Shafiei Sabet, P., and Sauer, D.U. (2017). Influence of operational condition on lithium plating for commercial lithium-ion batteries–electrochemical experiments and post-mortem-analysis. Applied energy *206*, 934–946.

15. Meda, U.S., Lal, L., Sushantha, M., and Garg, P. (2022). Solid electrolyte interphase (sei), a boon or a bane for lithium batteries: A review on the recent advances. J. Energy Storage *47*, 103564.

16. Heenan, T.M.M., Wade, A., Tan, C., Parker, J.E., Matras, D., Leach, A.S., Robinson, J.B., Llewellyn, A., Dimitrijevic, A., Jervis, R., et al. (2020). Identifying the origins of microstructural defects such as cracking within Ni-rich NMC811 cathode particles for lithium-ion batteries. Adv. Energy Mater. *10*, 2002655.

17. Wikner, E., Björklund, E., Fridner, J., Brandell, D., and Thiringer, T. (2021). How the utilised soc window in commercial Li-ion pouch cells influence battery ageing. Journal of Power Sources Advances *8*, 100054.

18. Spitthoff, L., Shearing, P.R., and Burheim, O.S. (2021). Temperature, ageing and thermal management of lithium-ion batteries. Energies *14*, 1248.

19. Guo, J., Li, Y., Meng, J., Pedersen, K., Gurevich, L., and Stroe, D.I. (2022). Understanding the mechanism of capacity increase during early cycling of commercial NMC/graphite lithium-ion batteries. J. Energy Chem. *74*, 34–44.

20. Cloos, L., Queisser, O., Chahbaz, A., Paarmann, S., Sauer, D.U., and Wetzel, T. (2024). Thermal transients to accelerate cyclic aging of lithium-ion batteries. Batter. Supercaps *7*, e202300445.

21. Chahbaz, A., Luo, Y., Stahl, G., Ditler, H., Jaumann, T., Glinka, M., Lingen, C., Sauer, D.U., and Li, W. (2024). Pressure-induced capacity recovery and performance enhancements in LTO/NMC-LCO batteries. Adv. Funct. Mater. *35*, 2419229.

22. Laufen, H., Berg, S., Engeser, J., Strautmann, M., Koprivc, A., Rahe, C., Figgemeier, E., and Sauer, D.U. (2024). Correlation between voltage, strain, and impedance as a function of pressure of a nickel-rich NMC lithium-ion pouch cell. Adv. Mater. Technol. *9*, 2301965.

23. Chahbaz, A., Meishner, F., Li, W., Ünlübayir, C., and Uwe Sauer, D. (2021). Non-invasive identification of calendar and cyclic ageing mechanisms for lithium-titanate-oxide batteries. Energy Storage Mater. *42*, 794–805.

24. Redondo-Iglesias, E., Venet, P., and Pelissier, S. (2018). Calendar and cycling ageing combination of batteries in electric vehicles. Microelectron. Reliab. *88–90*, 1212–1215.

25. Rücker, F., Schoeneberger, I., Wilmschen, T., Chahbaz, A., Dechent, P., Hildenbrand, F., Barbers, E., Kuipers, M., Figgener, J., and Sauer, D.U. (2022). A comprehensive electric vehicle model for vehicle-to-grid strategy development. Energies *15*, 4186.

26. Nikolian, A., Jaguemont, J., De Hoog, J., Goutam, S., Omar, N., Van Den Bossche, P., and Van Mierlo, J. (2018). Complete cell-level lithium-ion electrical ecm model for different chemistries (NMC, LFP, LTO) and temperatures (- 5 c to 45 c)–optimized modelling techniques. Int. J. Electr. Power Energy Syst. *98*, 133–146.

27. Gantenbein, S., Weiss, M., and Ivers-Tiffée, E. (2018). Impedance based time-domain modeling of lithium-ion batteries: Part i. J. Power Sources *379*, 317–327.

28. Andre, D., Meiler, M., Steiner, K., Walz, H., Soczka-Guth, T., and Sauer, D.u. (2011). Characterization of high-power lithium-ion batteries by electrochemical impedance spectroscopy. ii: Modelling. J. Power Sources *196*, 5349–5356.

29. Abraham, D.p., Kawauchi, S., and Dees, D.w. (2008). Modeling the impedance versus voltage characteristics of lini0. 8co0. 15al0. 05o2. Electrochim. Acta *53*, 2121–2129.

30. Illig, J., Ender, M., Weber, A., and Ivers-Tiffée, E. (2015). Modeling graphite anodes with serial and transmission line models. J. Power Sources *282*, 335–347.

31. Waag, W., Käbitz, S., and Sauer, D.U. (2013). Experimental investigation of the lithium-ion battery impedance characteristic at various conditions and aging states and its influence on the application. Applied energy *102*, 885–897.

32. Schmalstieg, J., Käbitz, S., Ecker, M., and Sauer, D.U. (2014). A holistic aging model for Li (NiMnCo) O_2 based 18650 lithium-ion batteries. J. Power Sources *257*, 325–334.

33. Sarasketa-Zabala, E., Martinez-Laserna, E., Berecibar, M., Gandiaga, I., Rodriguez-Martinez, L.M., and Villarreal, I. (2016). Realistic lifetime prediction approach for Li-ion batteries. Applied energy *162*, 839–852.

34. Petit, M., Prada, E., and Sauvant-Moynot, V. (2016). Development of an empirical aging model for Li-ion batteries and application to assess the impact of vehicle-to-grid strategies on battery lifetime. Applied energy *172*, 398–407.

35. Yang, X., Zhan, C., Xu, D., Nan, D., Lv, R., Shen, W., Kang, F., and Huang, Z.H. (2022). Siox@ Si-graphite microspheres for high-stable anode of lithium-ion batteries. Electrochim. Acta *426*, 140795.

36. Wildfeuer, L., Gieler, P., and Karger, A. (2021). Combining the distribution of relaxation times from EIS and time-domain data for parameterizing equivalent circuit models of lithium-ion batteries. Batteries *7*, 52.

37. Baronti, F., Zamboni, W., Femia, N., Roncella, R., and Saletti, R. (2013). Experimental analysis of open-circuit voltage hysteresis in lithium-iron-phosphate batteries. In IECON 2013: 39th Annual Conference of the IEEE Industrial Electronics Society (IEEE), pp. 6728–6733.

38. Wycisk, D., Oldenburger, M., Stoye, M.G., Mrkonjic, T., and Latz, A. (2022). Modified plett-model for modeling voltage hysteresis in lithium-ion cells. J. Energy Storage *52*, 105016.

39. Plett, G.L. (2004). Extended kalman filtering for battery management systems of LiPb-based hev battery packs: Part 2. modeling and identification. J. Power Sources *134*, 262–276. https://doi.org/10.1016/j.jpowsour.2004.02.032. https://www.sciencedirect.com/science/article/pii/S037877530400360X.

40. Paarmann, S., Schreiber, M., Chahbaz, A., Hildenbrand, F., Stahl, G., Rogge, M., Dechent, P., Queisser, O., Frankl, S.D., Morales Torricos,

P., et al. (2024). Short-term tests, long-term predictions–accelerating ageing characterisation of lithium-ion batteries. Batter. Supercaps *7*, e202300594.

41. Ecker, M., Gerschler, J.B., Vogel, J., Käbitz, S., Hust, F., Dechent, P., and Sauer, D.U. (2012). Development of a lifetime prediction model for lithium-ion batteries based on extended accelerated aging test data. J. Power Sources *215*, 248–257.
42. Saldaña Mulero, G., San Martín Díaz, J.I., Zamora Belver, I., Asensio De Miguel, F.J., Oñederra Leyaristi, O., and González Pérez, M. (2022). Empirical calendar ageing model for electric vehicles and energy storage systems batteries. J. Energy Storage *55*, 105676.
43. Hahn, S.L., Storch, M., Swaminathan, R., Obry, B., Bandlow, J., and Birke, K.P. (2018). Quantitative validation of calendar aging models for lithium-ion batteries. J. Power Sources *400*, 402–414.
44. Ali, H., Beltran, H., Lindsey, N.J., and Pecht, M. (2023). Assessment of the calendar aging of lithium-ion batteries for a long-term—space missions. Front. Energy Res. *11*, 1108269.
45. Torregrosa, A.J., Broatch, A., Olmeda, P., and Agizza, L. (2024). A semi-empirical model of the calendar ageing of lithium-ion batteries aimed at automotive and deep-space applications. J. Energy Storage *80*, 110388.
46. Pan, T., Li, Y., Yao, Z., Liu, S., Zhu, Y., Wang, X., Wang, J., Zheng, C., and Sun, W. (2025). Research advances on lithium-ion batteries calendar life prognostic models. Carbon Neutralization *4*, e192.
47. Mussa, A.S., Liivat, A., Marzano, F., Klett, M., Philippe, B., Tengstedt, C., Lindbergh, G., Edström, K., Lindström, R.W., and Svens, P. (2019). Fast-charging effects on ageing for energy-optimized automotive LiNi1/3Mn1/3Co1/3O2/graphite prismatic lithium-ion cells. J. Power Sources *422*, 175–184.
48. Sarasketa-Zabala, E., Gandiaga, I., Martinez-Laserna, E., Rodriguez-Martinez, L.m., and Villarreal, I. (2015). Cycle ageing analysis of a lifepo4/graphite cell with dynamic model validations: Towards realistic lifetime predictions. J. Power Sources *275*, 573–587.
49. Li, X., Colclasure, A.M., Finegan, D.P., Ren, D., Shi, Y., Feng, X., Cao, L., Yang, Y., and Smith, K. (2019). Degradation mechanisms of high capacity 18650 cells containing Si-graphite anode and nickel-rich NMC cathode. Electrochim. Acta *297*, 1109–1120.
50. Chen, T., Wu, J., Zhang, Q., and Su, X. (2017). Recent advancement of siox based anodes for lithium-ion batteries. J. Power Sources *363*, 126–144.
51. Witzenhausen, H., Kowal, J., and Sauer, D.U. (2017). Elektrische batteriespeichermodelle: Modellbildung, parameteridentifikation und modellreduktion. Tech. Rep. Institut für Stromrichtertechnik und Elektrische Antriebe (RWTH Aachen).
52. Illig, J., Schmidt, J.P., Weiss, M., Weber, A., and Ivers-Tiffée, E. (2013). Understanding the impedance spectrum of 18650 lifepo4-cells. J. Power Sources *239*, 670–679.
53. Shafiei Sabet, P., Stahl, G., and Sauer, D.U. (2020). Non-invasive investigation of predominant processes in the impedance spectra of high energy lithium-ion batteries with nickel–cobalt–aluminum cathodes. J. Power Sources *472*, 228189.
54. Cruz-Manzo, S., and Greenwood, P. (2020). An impedance model based on a transmission line circuit and a frequency dispersion Warburg component for the study of EIS in Li-ion batteries. J. Electroanal. Chem. *871*, 114305.
55. Illig, J., Ender, M., Chrobak, T., Schmidt, J.P., Klotz, D., and Ivers-Tiffée, E. (2012). Separation of charge transfer and contact resistance in LiFePo4-cathodes by impedance modeling. J. Electrochem. Soc. *159*, A952–A960.
56. Nurpeissova, A., Park, D.I., Kim, S.S., and Sun, Y.K. (2015). Epicyanohydrin as an interface stabilizer agent for cathodes of Li-ion batteries. J. Electrochem. Soc. *163*, A171–A177.
57. Steinhauer, M., Risse, S., Wagner, N., and Friedrich, K.A. (2017). Investigation of the solid electrolyte interphase formation at graphite anodes in lithium-ion batteries with electrochemical impedance spectroscopy. Electrochim. Acta *228*, 652–658.
58. Pan, K., Zou, F., Canova, M., Zhu, Y., and Kim, J.H. (2020). Comprehensive electrochemical impedance spectroscopy study of Si-based anodes using distribution of relaxation times analysis. J. Power Sources *479*, 229083.
59. Zhu, J., Knapp, M., Liu, X., Yan, P., Dai, H., Wei, X., and Ehrenberg, H. (2021). Low-temperature separating lithium-ion battery interfacial polarization based on distribution of relaxation times (DRT) of impedance. IEEE Trans. Transp. Electrific. *7*, 410–421.
60. Chen, X., Li, L., Liu, M., Huang, T., and Yu, A. (2021). Detection of lithium plating in lithium-ion batteries by distribution of relaxation times. J. Power Sources *496*, 229867.
61. Katzer, F., and Danzer, M.A. (2021). Analysis and detection of lithium deposition after fast charging of lithium-ion batteries by investigating the impedance relaxation. J. Power Sources *503*, 230009.
62. Lu, Y., Zhao, C.Z., Huang, J.Q., and Zhang, Q. (2022). The timescale identification decoupling complicated kinetic processes in lithium batteries. Joule *6*, 1172–1198.
63. Autofit development team. (2024). Autofit. GitHub. https://git.rwth-aachen.de/isea/ecmfitting.Gitlab.
64. Bihn, S., Rinner, J., Witzenhausen, H., Krause, F., Ringbeck, F., and Sauer, D.U. (2024). Physics-based equivalent circuit model motivated by the Doyle–Fuller–Newman model. Batteries *10*, 314.
65. López-Villanueva, J.A., Rodríguez-Iturriaga, P., Parrilla, L., and Rodríguez-Bolívar, S. (2022). A compact model of the ZARC for circuit simulators in the frequency and time domains. AEU-International Journal of Electronics and Communications *153*, 154293.
66. Cruz-Manzo, S., and Greenwood, P. (2022). Analytical transfer function to simulate the dynamic response of the finite-length warburg impedance in the time-domain. J. Energy Storage *55*, 105529.
67. Levi, M.D., and Aurbach, D. (1997). Simultaneous measurements and modeling of the electrochemical impedance and the cyclic voltammetric characteristics of graphite electrodes doped with lithium. J. Phys. Chem. B *101*, 4630–4640.
68. Weber, R., Louli, A.J., Plucknett, K.P., and Dahn, J.R. (2019). Resistance growth in lithium-ion pouch cells with LiNi0.80Co0.15Al0.05O2 positive electrodes and proposed mechanism for voltage dependent charge-transfer resistance. J. Electrochem. Soc. *166*, A1779–A1784.
69. Knorr, J., Gomez-Martin, A., Hsiao, H.C., Adam, A., Rödl, B., and Danzer, M.A. (2024). Effect of different charge rates on the active material lithiation of Gr/SiOx blend anodes in lithium-ion cells. J. Energy Storage *86*, 111151.
70. Yao, K.P.C., Okasinski, J.S., Kalaga, K., Almer, J.D., and Abraham, D.P. (2019). Operando quantification of (de) lithiation behavior of silicon–graphite blended electrodes for lithium-ion batteries. Adv. Energy Mater. *9*, 1803380.
71. Zilberman, I., Sturm, J., and Jossen, A. (2019). Reversible self-discharge and calendar aging of 18650 nickel-rich, silicon-graphite lithium-ion cells. J. Power Sources *425*, 217–226.
72. Heugel, P., Märkle, W., Deich, T., von Kessel, O., and Tübke, J. (2022). Thickness change and jelly roll deformation and its impact on the aging and lifetime of commercial 18650 cylindrical Li-ion cells with silicon containing anodes and nickel-rich cathodes. J. Energy Storage *53*, 105101.
73. Schmitt, J., Horstkötter, I., and Bäker, B. (2024). A novel approach for modelling voltage hysteresis in lithium-ion batteries demonstrated for silicon graphite anodes: Comparative evaluation against established preisach and plett model. Journal of Power Sources Advances *26*, 100139.
74. Iseaframe development team. Iseaframe (2022). Gitlab. https://git.rwth-aachen.de/isea/framework.Gitlab.
75. Hust, F.E., Ascheid, G., and Sauer, D.U. (2019). Physico-chemically motivated parameterization and modelling of real-time capable lithium-ion

battery models: a case study on the tesla model s battery. Institut für Stromrichtertechnik und Elektrische Antriebe (Tech. Rep.).

76. Barbers, E., Hust, F.E., Hildenbrand, F.E.A., Frie, F., Quade, K.L., Bihn, S., Sauer, D.U., and Dechent, P. (2024). Exploring the effects of cell-to-cell variability on battery aging through stochastic simulation techniques. J. Energy Storage *84*, 110851.
77. Hildenbrand, F., Ditscheid, D., Barbers, E., and Sauer, D.U. (2023). Influence of the anode overhang on the open-circuit voltage and the ageing of lithium-ion batteries—a model based study. Appl. Energy *332*, 120395.
78. Murashko, K.A., Pyrhönen, J., and Jokiniemi, J. (2020). Determination of the through-plane thermal conductivity and specific heat capacity of a Li-ion cylindrical cell. Int. J. Heat Mass Tran. *162*, 120330.
79. Jiang, Y., Huang, J., Xu, P., and Wang, P. (2023). Axial and radial thermal conductivity measurement of 18,650 lithium-ion battery. J. Energy Storage *72*, 108516.
80. Ma, S., Jiang, M., Tao, P., Song, C., Wu, J., Wang, J., Deng, T., and Shang, W. (2018). Temperature effect and thermal impact in lithium-ion batteries: A review. Prog. Nat. Sci. Mater. Int. *28*, 653–666.
81. Gholami, J., and Barzoki, M.F. (2021). Electrochemical modeling and parameter sensitivity of lithium-ion battery at low temperature. J. Energy Storage *43*, 103189.
82. Iurilli, P., Brivio, C., Carrillo, R., and Wood, V. (2022). Eis2mod: A drt-based modeling framework for Li-ion cells. IEEE Trans. Ind. Appl. *58*, 1429–1439.
83. Bozorgchenani, M., Kucinskis, G., Wohlfahrt-Mehrens, M., and Waldmann, T. (2022). Experimental confirmation of C-rate dependent minima shifts in Arrhenius plots of Li-ion battery aging. J. Electrochem. Soc. *169*, 030509.
84. Nikolov, N.I., Chahbaz, A., Hildenbrand, F., Kateri, M., and Sauer, D.U. (2024). Statistical investigation of temperature-dependent cycle lifetime and cell-to-cell variance in lithium-ion batteries: A model-based approach. J. Power Sources *623*, 235334.
85. Werner, D., Paarmann, S., Wiebelt, A., and Wetzel, T. (2020). Inhomogeneous temperature distribution affecting the cyclic aging of Li-ion cells. part ii: Analysis and correlation. Batteries *6*, 12.
86. Karger, A., O'Kane, S.E.J., Rogge, M., Kirst, C., Singer, J.P., Marinescu, M., Offer, G.J., and Jossen, A. (2024). Modeling particle versus sei cracking in lithium-ion battery degradation: Why calendar and cycle aging cannot simply be added. J. Electrochem. Soc. *171*, 090512.
87. Watanabe, S., Kinoshita, M., Hosokawa, T., Morigaki, K., and Nakura, K. (2014). Capacity fading of $LiAl_yNi_{1-x-y}Co_xO_2$ cathode for lithium-ion batteries during accelerated calendar and cycle life tests (effect of depth of discharge in charge–discharge cycling on the suppression of the micro-crack generation of $LiAl_yNi_{1-x-y}Co_xO_2$ particle). J. Power Sources *260*, 50–56.
88. Keil, P., and Jossen, A. (2017). Impact of dynamic driving loads and regenerative braking on the aging of lithium-ion batteries in electric vehicles. J. Electrochem. Soc. *164*, A3081–A3092.
89. Lu, M., Zhang, X., Ji, J., Xu, X., and Zhang, Y. (2020). Research progress on power battery cooling technology for electric vehicles. J. Energy Storage *27*, 101155.
90. Schreiber, M., Lin, Y., Sommer, A., Wassiliadis, N., Morales Torricos, P., Rogge, M., Lewerenz, M., Grosu, C., Endisch, C., Jossen, A. et al. (2025). Apparent vs. true battery aging: Impact of various load characteristics on accelerated aging tests. True Battery Aging: Impact of Various Load Characteristics on Accelerated Aging Tests.Journal of Energy Storage,127, 116924
91. Rogge, M., and Jossen, A. (2024). Path-dependent ageing of lithium-ion batteries and implications on the ageing assessment of accelerated ageing tests. Batteries & Supercaps *7*, e202300313.
92. Schreiber, M., Steiner, T., Kayl, J., Schönberger, B., Grosu, C., and Lienkamp, M. (2025). The overlooked role of battery cell relaxation: How reversible effects manipulate accelerated aging characterization. World Electr. Veh. J. *16*, 255.
93. Morales Torricos, P., Endisch, C., and Lewerenz, M. (2023). Apparent aging during accelerated cycling aging test of cylindrical silicon containing Li-ion cells. Batteries *9*, 230.
94. Schreiber, M., Abo Gamra, K., Bilfinger, P., Teichert, O., Schneider, J., Kröger, T., Wassiliadis, N., Ank, M., Rogge, M., Schöberl, J., et al. (2024). Understanding lithium-ion battery degradation in vehicle applications: Insights from realistic and accelerated aging tests using volkswagen id. 3 pouch cells. J. Energy Storage *112*, 115357.
95. Wildfeuer, L., Karger, A., Aygül, D., Wassiliadis, N., Jossen, A., and Lienkamp, M. (2023). Experimental degradation study of a commercial lithium-ion battery. J. Power Sources *560*, 232498.
96. Kuntz, P., Raccurt, O., Azaïs, P., Richter, K., Waldmann, T., Wohlfahrt-Mehrens, M., Bardet, M., Buzlukov, A., and Genies, S. (2021). Identification of degradation mechanisms by post-mortem analysis for high power and high energy commercial Li-ion cells after electric vehicle aging. Batteries *7*, 48. https://doi.org/10.3390/batteries7030048.
97. Willenberg, L.K., Dechent, P., Fuchs, G., Sauer, D.U., and Figgemeier, E. (2020). High-precision monitoring of volume change of commercial lithium-ion batteries by using strain gauges. Sustainability *12*, 557.
98. Stiaszny, B., Ziegler, J.C., Krauß, E.E., Schmidt, J.P., and Ivers-Tiffée, E. (2014). Electrochemical characterization and post-mortem analysis of aged LiMn2O4–Li (Ni0.5Mn0.3Co0.2)O2/graphite lithium ion batteries. Part I: Cycle aging. J. Power Sources *251*, 439–450.
99. Ciucci, F., and Chen, C. (2015). Analysis of electrochemical impedance spectroscopy data using the distribution of relaxation times: A bayesian and hierarchical bayesian approach. Electrochim. Acta *167*, 439–454.
100. Wan, T.H., Saccoccio, M., Chen, C., and Ciucci, F. (2015). Influence of the discretization methods on the distribution of relaxation times deconvolution: implementing radial basis functions with drttools. Electrochim. Acta *184*, 483–499.
101. Hahn, M., Rosenbach, D., Krimalowski, A., Nazarenus, T., Moos, R., Thelakkat, M., and Danzer, M.A. (2020). Investigating solid polymer and ceramic electrolytes for lithium-ion batteries by means of an extended distribution of relaxation times analysis. Electrochim. Acta *344*, 136060.
102. Plank, C., Rüther, T., Jahn, L., Schamel, M., Schmidt, J.P., Ciucci, F., and Danzer, M.A. (2023). A review on the distribution of relaxation times analysis: A powerful tool for process identification of electrochemical systems. J. Power Sources *594*, 233845.
103. Frie, F., Ditler, H., Klick, S., Stahl, G., Rahe, C., Ghaddar, T., and Sauer, D.U. (2024). An analysis of calendaric aging over 5 years of Ni-rich 18650-cells with Si/C anodes. Chemelectrochem *11*, e202400020.
104. Willenberg, L., Dechent, P., Fuchs, G., Teuber, M., Eckert, M., Graff, M., Kürten, N., Sauer, D.U., and Figgemeier, E. (2020). The development of jelly roll deformation in 18650 lithium-ion batteries at low state of charge. J. Electrochem. Soc. *167*, 120502.
105. Willenberg, L. (2020). Volumenausdehnung und ihre auswirkungen auf die alterung einer zylindrischen lithium-ionen-batterie (Rheinisch-Westfälische Technische Hochschule Aachen), p. 2020. Ph.D. thesis Dissertation.
106. Wassiliadis, N., Steinsträter, M., Schreiber, M., Rosner, P., Nicoletti, L., Schmid, F., Ank, M., Teichert, O., Wildfeuer, L., Schneider, J., et al. (2022). Quantifying the state of the art of electric powertrains in battery electric vehicles: Range, efficiency, and lifetime from component to system level of the volkswagen id. 3. Etransportation *12*, 100167.
107. Jöst, D., Blömeke, A., Sauer, D.U., and Ringbeck, F. (2021). Timeseries data of a drive cycle aging test of 28 high energy NCA/C+Si round cells of type 18650. Tech. Rep. Institut für Stromrichtertechnik und Elektrische Antriebe (RWTH Aachen). https://doi.org/10.18154/RWTH-2021-02814.
108. Marino, S., Hogue, I.B., Ray, C.J., and Kirschner, D.E. (2008). A methodology for performing global uncertainty and sensitivity analysis in systems biology. J. Theor. Biol. *254*, 178–196.
109. Zar, J.H. (2005). Spearman Rank Correlation, *7* (Encyclopedia of biostatistics).